Ph.D. DISSERTATION

High-sensitive Low Power Tunneling Field Effect Transistor Biosensor for Multiplexed Sensing Application

다중 감지를 위한 고감도 저전력 터널링 전계효과 트랜지스터 바이오 센서

BY

DAE WOONG KWON

February 2017

DEPARTMENT OF ELECTRICAL AND
COMPUTER ENGINEERING
COLLEGE OF ENGINEERING
SEOUL NATIONAL UNIVERSITY

High-sensitive Low Power Tunneling Field Effect Transistor Biosensor for Multiplexed Sensing Application

다중 감지를 위한 고감도 저전력 터널링 전계효과 트랜지스터 바이오 센서

指導敎授 朴炳國

이 論文을 工學博士學位論文으로 提出함

2017 년 2 월

서울大學校 大學院

電氣·情報 工學部

權 大 雄

權大雄의 工學博士 學位論文을 認准함

2017 년 2 월

委 員 長 : 박영준 (印)

副委員長 : 박병국 (印)

委 員 : 이종호 (印)

委 員 : 정인영 (印)

委 員 : 김대환 (印)

Abstract

As fabrication technology has continued to develop, various nano-size biomedical sensors have been widely researched since the size of biological entities, such as DNA, proteins, and viruses are similar to their size. Especially, chemical and biomedical sensors using fluorescent labeling and parallel optical detection techniques have received much attention for high sensitivity. However, they have a number of drawbacks such as expensive and time-consuming processes for sample preparation and data analysis.

To overcome these limitations, silicon nanowire (SiNW) Ion Sensitive Field Effect Transistors (ISFET) have been proposed as one of the most promising chemical/biomedical sensors since it has good characteristics such as label-free, real-time detection, and excellent sensitivity caused by high surface-to-volume ratio. In terms of the fabrication process, SiNW ISFETs also have compatibility with CMOS technology. Various fabrication methods of SiNW ISFETs have been reported. Recently, our group demonstrated a novel SiNW MOSFET sensor which can be integrated with a CMOS device by using top-down fabrication process. However, the proposed top-down process cannot avoid the damage of the sensing material by the plasma damage because the sensing area is formed by the dry-etch process, which leads to the degradation of the sensitivity and the current drift. Furthermore, it is impossible to fine-tune the various

threshold voltages (V_{th}) of the circuit devices by the implant process, which results in circuit malfunction and reduction in amplification factor.

In this thesis, the novel top-down approached fabrication method using top SiO_2-SiN-bottom SiO_2 (ONO) dielectric stacks is proposed and implemented to obtain sensors with defect-free sensing oxide and V_{th}-tunable devices in CMOS read-out circuits. By wet-etching the top SiO_2 and the SiN, the sensor with defect-free sensing oxide is obtained. Also, the V_{th}-tunable circuit devices with the ONO stacks are simultaneously achieved by protecting the ONO stacks from the wet-etching. Through the measurements of pH response and current drift in the sensor and program operations in the circuit device, it is confirmed that the pH/biomolecule response and the current drift of the sensor are improved and the V_{th} of the circuit device can be fine-controlled.

Although the defect-free sensing material improves the drift and the sensitivity, the MOSFET sensor has a theoretical limitation on the maximum sensitivity because MOSFETs cannot implement sub-60mV/dec SS at room temperature. To achieve the higher sensitivity, a TFET sensor is proposed and fabricated since it can achieve sub-kT/qS at room temperature by using band-to-band tunneling as carrier injection mechanism. From TCAD simulations, it is revealed that the TFET sensor has two I_D saturations by the saturation of the source-to-channel tunneling width and the drain-side carrier injection. Moreover, it is experimentally confirmed that the TFET sensor is the superior sensitivity up to the first I_D saturation region and there is no difference in sensitivity from the second I_D saturation region as compared to the MOSFET sensor.

Finally, the possibility of multiplexed sensing is verified with the fabricated MOSFET and TFET sensors. To form two different sensing materials reacted with GBP-Ala/Anti-AI and SBP-H1N1/Anit-H1N1 for the multiplexed-sensing, gold is partially covered on the SiO_2 by a lift-off process. Then, the changes of saturation and GIDL current are monitored in the MOSFET sensor after the reactions of GBP-Ala/Anti-AI (SBP-H1N1/Anit-H1N1) to the gold (SiO_2). Two different biomolecules are independently detected by the changes in the saturation and the GIDL currents. To solve the problems of the MOSFET sensor by the dependence of the gold formation position on the sensitivity and the large current difference between the saturation and the GIDL currents, the changes of tunneling and ambipolar currents are measured in the TFET sensor. As a result, it is revealed that two different biomolecules can be detected without interference regardless of the position of the gold layer by the changes of the tunneling and ambipolar currents with almost equivalent current level.

Key Words: defect-free sensing material in ISFET, tunnel field-effect transistor biosensor, multiplexed sensing.

Student Number: 2014-30316

Contents

Chapter 1

Introduction

1.1 SiNW ISFET Co-integrated with CMOS Read-out Circuits

As fabrication technology has continued to develop, various nano-size biomedical sensors have been widely researched since the size of biological entities, such as DNA, proteins, and viruses are similar to their size [1], [2]. Especially, biomedical sensors using fluorescent labeling and parallel optical detection techniques have received much attention for high sensitivity [3]. However, they have a number of drawbacks such as expensive and time-consuming processes for sample preparation and data analysis. To overcome these limitations, silicon nanowire (SiNW) Ion Sensitive Field Effect Transistors (ISFET) have been proposed as one of the most promising biomedical sensors since it has good characteristics such as label-free, real-time detection, and excellent sensitivity caused by high surface-to-volume ratio [4]

In terms of the fabrication process, the early stage of SiNW biosensors had been studied through a bottom-up approach [5]-[8]. However, the bottom-up approach has serious disadvantages in the reproducibility of the fabrication process and device design since it is difficult to control doping concentration and dimension parameters which affect the electrical performance of the device. Also, it is not suitable to be integrated with a mature complementary metal-oxide semiconductor (CMOS) technology and circuitry because SiNWs fabricated by the bottom-up process cannot be well-aligned with electrodes. Meanwhile, a top-down approach can produce uniformly distributed and well-aligned NWs in predetermined orientation and position on a substrate. Thus, many researchers have demonstrated CMOS-compatible biosensors by using top-down processed NWs [9]-[18]. Although the possibility of the integration with mature state-of-the-art CMOS technology and circuitry has been argued in the previous works on the top-down CMOS-compatible biosensors, the real integration of top-down approached SiNW biosensors with CMOS technology and circuit has been rarely reported. Furthermore, most previous works have adopted the lift-off process which is not compatible with the conventional CMOS back-end process. Thus, for assessing real advantages of SiNW-CMOS hybrid systems and expediting their wafer-scale mass-productions, the SiNW biosensors should be integrated with CMOS circuits by using the back-end process compatible with the conventional CMOS technology. Recently, our group demonstrated a novel high-sensitive SiNW biosensor which was co-integrated with CMOS circuit by using top-down approached and CMOS-compatible back-end

process simultaneously [19], [20].

1.2 Issues in Top-down Approached SiNW-CMOS Hybrid System

In the view point of the application of the co-integrated ISFET with CMOS circuit, there are still challenges on the path to commercialization as chemical and biomedical sensors. Particularly, the current drift (change of drain current under a fixed bias as a function of measurement time) has been considered to be one of the critical obstacles because it is almost impossible to read precise current value within limited sensing time [21]. In the previous studies [22]-[24], it has been reported that the drift of drain current (I_D) is mainly caused by the diffusion of ions into damaged sensing material. Unfortunately, the top-down process proposed by our group cannot avoid the damage of the sensing material by the plasma damage because the sensing area, where the SiNW surface contacts with the biomolecules, is formed by the dry-etch process.

In the SiNW-CMOS hybrid system, the threshold voltages (V_{th}) of the devices in read-out circuits, which convert a current change of a sensor by a biomolecule reaction to an output voltage, directly affects output voltage amplification. However, it is impossible to fine-tune the various V_{th}s of the devices by the implant process, which results in circuit malfunction and reduction in amplification factor. Thus, the fabrication method by which damage-free sensing material and read-out circuits composed of V_{th}-tunable

devices can be simply obtained should be introduced.

1.3 Sensitivity Improvement

The principle of electrical detection in ISFET sensors is based on the gating effect of the charged biomolecules on the sensing material such as gate oxide, which can be converted directly to the change in electrical properties such as current, conductance, and threshold voltage (V_{th}) [25], [26]. However, conventional FET-based biosensors (MOSFET biosensor) have a theoretical limitation on the maximum sensitivity because MOSFET cannot implement sub-60mV/dec subthreshold swing (SS) at room temperature [27].

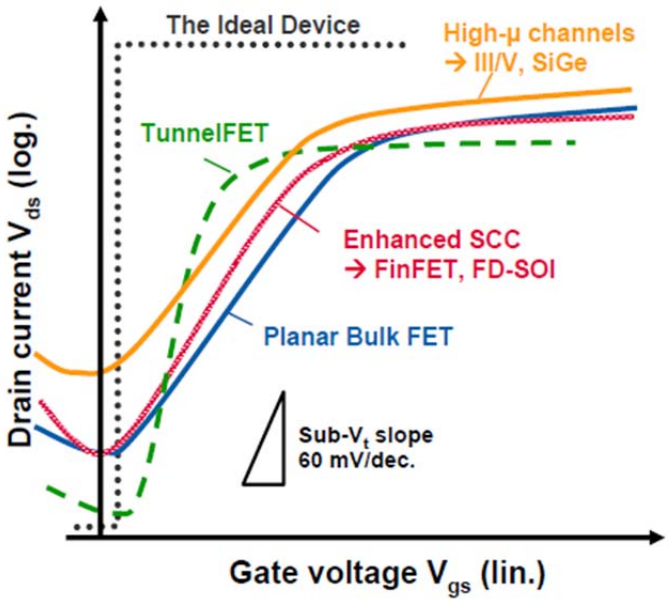

Fig. 1.1 The switching properties of various MOSFETs and TFET.

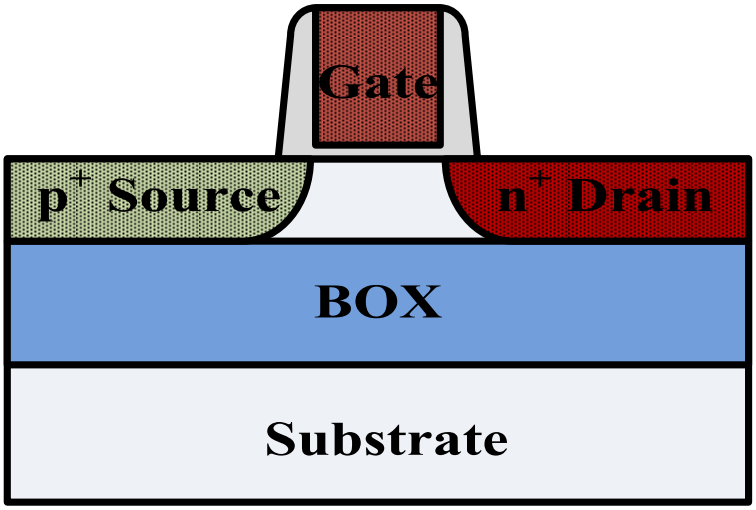

Fig. 1.2 The scheme of n-type TFET

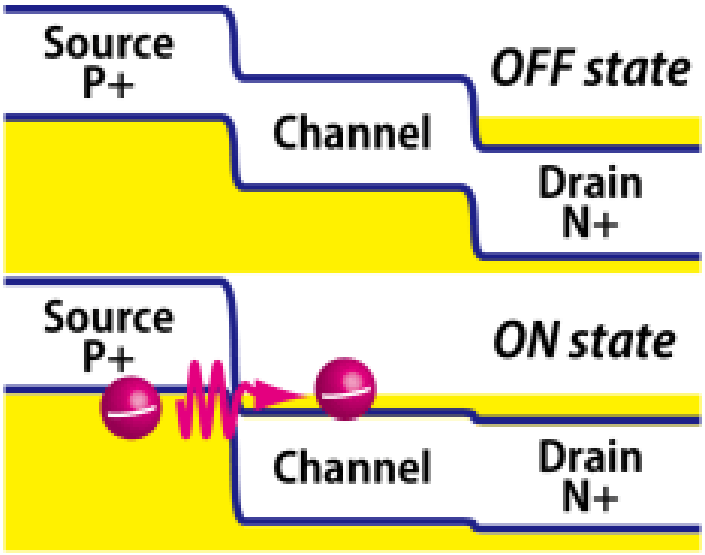

Fig. 1.3 The energy band diagrams of OFF state (V_{GS} = 0 V, V_{DS} = V_{DD}) and ON state (V_{GS} > V_{th}, V_{DS} = V_{DD}) in n-type TFET.

Inter-band tunnel field-effect transistors (TFET) have been extensively investigated because it can achieve sub-kT/qS at room temperature and enable supply voltage (V_{DD}) reduction for low-power logic applications as shown in Fig.1.1 [28]-[30]. TFET operation is based on band-to-band tunneling (BTBT) mechanism where electrons in the valence band of the source region pass through the barrier to the conduction band of the channel region. Thus, it has very small leakage current due to potential barrier. The basic structure of TFETs consists of a gated p-i-n diode where the source and the drain have asymmetric dopant type as shown in Fig.1.2 (n-type TFET). For principle operations, Figure 1.3 shows the energy band diagrams in ON/OFF states of TFET. When the device is in the OFF state, the electrons in the valence band of the source region can't be passed to empty states in the conduction band of the channel region by the energy barrier. Hence, turn-off current (I_{OFF}) is mostly determined by Shockley-Read-Hall (SRH) generation or recombination. As the positive gate voltage (V_{GS}) is applied, the conduction band of the channel region starts to go down. When the conduction band of the channel region is placed below the valence band of the source region, electrons can move to empty states in the channel region via BTBT, resulting in a sudden increase of the drain current. Therefore, carriers in the TFET are unaffected by thermal energy unlike MOSFET and SS can be lower than 60 mV/dec at room temperature in the consequence. These advantages of TFET devices can also be applied to biosensors and thus TFET sensors can have the possibility for improved sensitivity over MOSFET sensors with the lower power consumption.

1.4 Scope of Thesis

The first objective of this work is to propose and implement the novel fabrication method by which damage-free sensing material and read-out circuits composed of V_{th}-tunable devices can be simply obtained. The second objective is to implement a TFET sensor with higher sensitivity than MOSFET sensors by applying the proposed process and to verify the high sensitivity experimentally through electrical characteristics measurements. Furthermore, the work aims to maximize V_{out} change as a response to biomolecules by co-integrating MOSFET/TFET sensors with defect-free sensing material and V_{th}-tunable CMOS read-out circuit. The final objective is to implement a multiplexed sensing system that can independently monitor two different biomolecules simultaneously from one sensor by using proposed MOSFET/TFET sensors-CMOS hybrid system.

In Chapter 2, Top-down approached fabrication process methods and process conditions for the co-integration of MOSFET/TFET sensors and CMOS read-out circuits have been proposed, and core processes directly related to the performance of the sensors such as electron beam (e-beam) lithography for active formation, polycrystalline silicon gate etching, gate ion implantation, and sensing region formation are tested to confirm the detailed conditions of the critical unit processes. Before the pH/biomolecules sensing experiments with the fabricated devices, the successful processing of the fabricated SiNW sensors is confirmed through SEM and TEM analysis. Then, the surface treatment of the sensing material for pH sensing is carried out and the

measurement system for pH/biomolecules sensing is established.

In Chapter 3, the novel fabrication method using top oxide-nitride-bottom oxide (ONO) dielectric stacks is proposed and implemented to obtain sensors with defect-free sensing oxide and V_{th}-tunable devices in CMOS read-out circuits. The etching rate of SiO_2/SiN is first confirmed during H_3PO_4/HF wet-etching, respectively. Then, the sensors with the defect-free sensing oxide are achieved by removing top SiO_2 and SiN from the sensors with the ONO stacks based on the test results. The electrical characteristics such as pH response and I_D drift are measured in the fabricated sensors with the defect-free sensing oxide. Moreover, the V_{th}-tunability and the retention characteristics of the co-integrated circuit devices are also measured. Finally, V_{out} response as a converted result of I_D change by biomolecules is extracted from common source amplifier (CSA) circuit composed of one sensor and one n-type MOSFET.

In Chapter 4, a TFET sensor is proposed as a candidate with higher sensitivity than MOSFET sensors. To verify the validity of the TFET sensor, TCAD simulations are performed in terms of sensitivity. Furthermore, it is experimentally confirmed that the TFET sensor can have the higher sensitivity at SS and saturation regions by comparing the sensitivities between the fabricated MOSFET and TFET sensors.

In Chapter 5, the multiplexed-sensing method by which two different biomolecules can be independently detected in one sensor is introduced. To form two different sensing materials for the multiplexed-sensing, gold is partially covered on the SiO_2 by a lift-off process. The changes of V_{th} and gate-induced drain leakage (GIDL) current are

monitored in the MOSFET sensor after GBP-Ala/Anti-AI (SBP-H1N1/Anit-H1N1) is attached to the gold (SiO_2). Also, the changes of tunneling and ambipolar currents are measured in the TFET sensor after the antigen-antibody reactions on the gold and the SiO_2.

Finally, this work is concluded with the summary and the suggestions for future works in Chapter 6.

Chapter 2

Process Flow and Biomolecules/ pH Measurement Setting

2.1 Process Flow of Top-down Approached MOSFET/TFET sensors-CMOS Hybrid System

Various fabrication methods of SiNW FET sensors have been demonstrated. However, simple, low cost, and CMOS-compatible top-down fabrication process has not been demonstrated until recently. The proposed process flow of the SiNW sensors by our group is almost the same as that of MOSFETs. Except for the opening of the sensing area, all the other processes can be conducted simultaneously with MOSFETs. Considering the co-integration with MOSFETs, the equipment and conditions for the sensor fabrication should be the same as those of MOSFETs. Thus, conventional 0.25 μm process technology and e-beam lithography are used for the fabrication of the SiNW sensor.

The SiNW MOSFET/TFET sensors were fabricated on a 6-inch silicon-on-

insulator (SOI) wafer doped with boron (B^+) at a concentration of 4×10^{15} cm^{-3}. The silicon of the SOI wafer is 100 nm thick, and the thickness of the silicon oxide film used as the bottom insulator is 375 nm. Figure 2.1 shows the detailed process flow for integrating the SiNW MOSFET/TFET sensors with CMOS read-out circuits. The sequence of the process proceeds as follows.

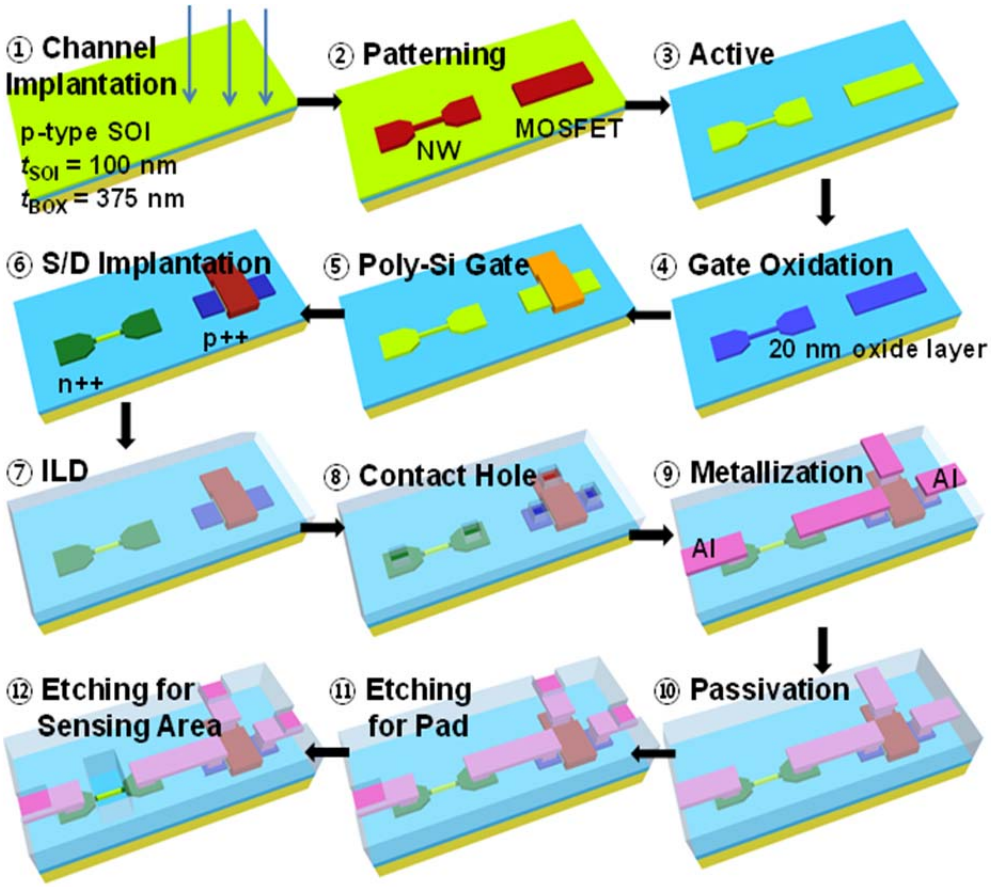

Fig. 2.1 Fabrication process flow of co-integrating MOSFET/TFET sensor and CMOS read-out circuit.

① Channel ion implantation: A 20 nm thick silicon oxide (SiO_2) film is deposited by dry oxidation process to prevent surface damage from ion implantation. As a result, the uppermost silicon is consumed by the oxidation process and reduced to a thickness of 90 nm. Then, B^+ is implanted into the channel of the n-type MOSFET sensor and device at a concentration of 5×10^{13} cm^{-2} with the energy of 20 keV. In the channel of the p-type MOSFET sensor and device, phosphorus (P^+) is implanted at 3×10^{13} cm^{-2} with the energy of 40 keV. The channel of the TFET sensor and device is blocked with a mask to prevent the ion implantation. After the ion implantation process, the uppermost silicon oxide film is removed from the hydrofluoric acid solution.

② Mask patterning: The active region of SiNWs and devices in read-out circuits is simultaneously defined on the wafer through a mix-and-match method that involves e-beam lithography and photolithography. Especially, the SiNW masks are formed by using the e-beam lithography from 30 nm to 300 nm.

③ Active area etching: This is the step of forming the pattern worked in process ② through silicon etching. As the etching mask, a general photoresist (PR) and hydrogen silsesquioxane (HSQ) are used. A 90 nm thick silicon layer is etched in inductively coupled plasma (ICP) equipment using hydrogen bromide (HBr) and oxygen (O_2).

④ Oxidation: A 10 nm thick gate oxide is grown on the active region through a dry oxidation process. As a result, the SiNW thickness of the sensor is reduced. An additional 10 nm thick oxide film is then deposited by low-pressure chemical vapor deposition (LPCVD) at 780 ℃. This silicon oxide film layer is used as a gate insulator

of devices in CMOS read-out circuits.

⑤ Polysilicon gate formation: After the oxidation process, 100 nm thick polycrystalline silicon (poly-Si) is deposited by a LPCVD process at the temperature of 630 °C. After the mask of the gate is processed by the photolithography process, the gate is formed by ICP etching. During the gate etching, all the poly-Si in the sensor region is removed, and the poly-Si gate not-etched by the mask is utilized as the gates of devices in CMOS read-out circuits.

⑥ Source/drain/gate ion implantation: ions are injected into the source/drain of the sensor and the source/drain/gate regions of the circuit devices, except for the SiNW channel where the ion implantation has previously been performed in process ①. In the case of n-type MOSFET sensors and circuit devices, arsenic (As^+) ions are implanted into the source/drain whereas the source/drain of p-type MOSFET sensors and circuit devices are implanted with boron difluoride ($BF2^+$) ions. In the case of the TFET sensor, ions are implanted by using the source and drain masks, respectively. The $BF2^+$ ions are implanted into the source and As^+ ions are injected into the drain. As^+ ions are implanted into the gate of the n-type circuit devices and $BF2^+$ ions are implanted into the gate of the p-type device. After removing the PR on the channel formed to prevent ion implantation of the SiNW channel, the heat treatment process is performed at 1000 °C for 30 minutes to activate the impurities.

⑦ Interlayer dielectric (ILD) and planarization (CMP) processes: The back-end process of SiNW MOSFET/TFET sensors is similar to a typical CMOS process. A 500 nm thick

interlayer dielectric is deposited by high density chemical vapor deposition (HDPCVD) and the surface of the ILD is planarized by a CMP process.

⑧ Contact Hole: After the planarization process, contact holes are formed through photolithography and CHF_3/CF_4 plasma reactive ion etching.

⑨ Metallization: An aluminum (Al) electrode is formed by Al deposition using sputtering, photolithography, and BCl_2/Cl_2 plasma reactive ion etching processes.

⑩ Passivation: Tetraethyl orthosilicate (TEOS) is deposited as a passivation layer to protect the CMOS circuitry and metal lines.

⑪ Pad: To measure devices and circuits on the 6-inch wafer, the oxide film on top of the metal pad connected to the device is removed by reactive ion etching.

⑫ Sensing area formation: A sensing area is formed on the SiNW. Since the sensing area is the region where the surface of the SiNW is in contact with the biomolecules, the oxide film on the SiNW should be removed. Therefore, the passivation oxide of TEOS is removed by CHF_3/CF_4 plasma reactive ion etching. However, excessive etching can lead to the damage to the SiNWs. Thus, the damage of the nanowires is minimized by etching the TEOS oxide film for a certain period of time and examining the thickness of the remaining oxide film. Finally, the process is terminated by an alloy process in a hydrogen atmosphere.

Figure 2.2(a) shows a cross-sectional view of the final SiNW MOSFET/TFET sensor and CMOS read-out circuit. Also, Fig. 2.2(b) demonstrates the top views and the device parameters of the sensor.

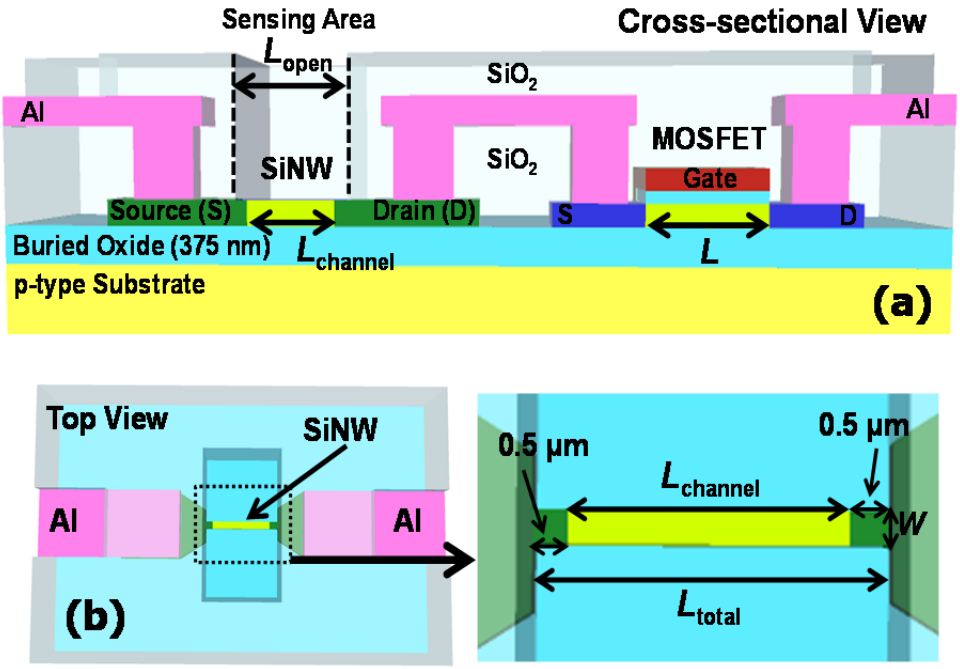

Fig. 2.2 (a) A cross-sectional view of the final SiNW MOSFET/TFET sensor and CMOS read-out circuit. (b) Top views of the sensor.

2.2 Fabrication Test of Critical Unit Process

Core processes directly related to the performance of the sensors are tested to confirm the detailed conditions of the critical unit processes. The first key process is the formation of nanowires to be used as channels in sensor devices. It is necessary to confirm that the pattern is not collapsed at designed line widths and maintains its own shape in accordance with the e-beam density (dose) when the e-beam patterning process is performed. The e-beam concentration is adjusted to 700 ~ 1300 μC/cm^2. The shape

and collapse of the nanowires are tested. Figure 2.3 shows SEM images of nanowires with 50 nm line width formed at the e-beam concentrations of 700 and 1100 μC/cm^2, respectively. At the e-beam concentration of 700 μC/cm^2, the line width of the nanowire is smaller than intended one and the nanowire is collapsed elsewhere. However, the intended line width of 50 nm is well implemented at the e-beam concentration of 1100 μC/cm^2. Based on this information, the e-beam concentration at the actual process is set to 1100 μC/cm^2 and the e-beam pattern process is carried out.

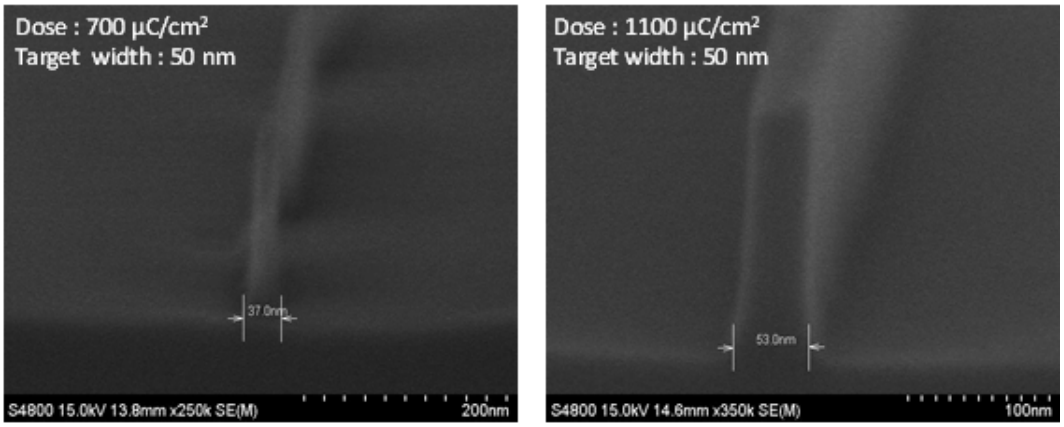

Fig. 2.3 SEM images of nanowire patterns formed at various e-beam doses.

The second key process is polycrystalline silicon (poly-Si) gate formation. When the poly-Si gate is etched after deposition, the nanowire of the sensor may be damaged if the poly-Si is too over-etched. However, if it is under-etched, the poly-Si remains and the source/gate/drain may not be isolated. Therefore, it is necessary to select the optimum time for etching the poly-Si. Scanning electron microscopy (SEM) analysis

indicates that the poly-Si is completely etched and the nanowires are safely protected without damage by ~15% (15 nm) additional etching of the entire poly-Si thickness. Figure 2.4 is the SEM image after the poly-Si etching. The dotted line in the image shows the remaining oxide film on the channel surface, confirming that the channel do not have damage though the poly-Si is completely removed. Based on the test results, ~15% additional etching of the entire gate thickness is applied in the actual process.

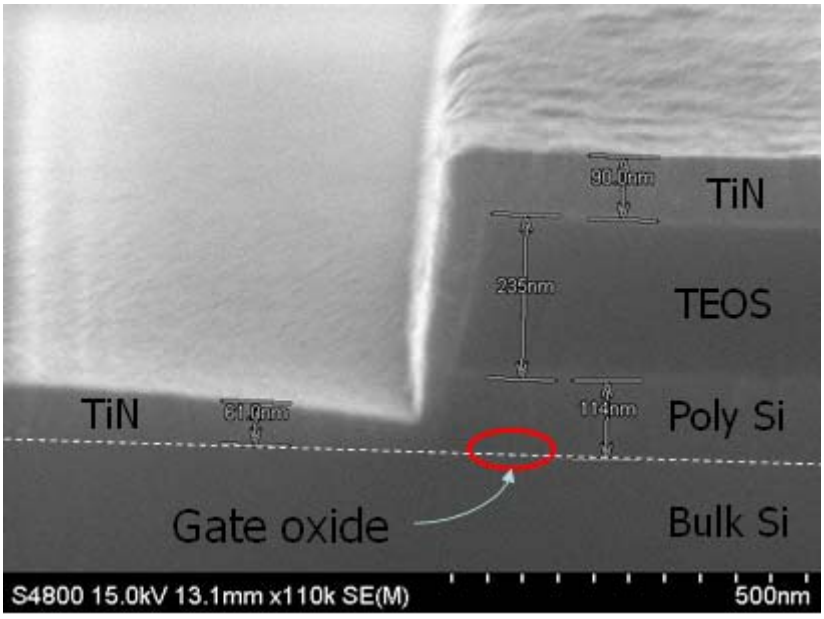

Fig. 2.4 SEM image after poly-Si gate etching.

The third key process is gate ion implantation. Since the formed poly-Si gate has a thickness of about 100 nm, ions must penetrate to the lowermost end of the gate (poly-Si contacting the oxide film on the channel) during ion implantation so that it can serve

as a gate. In order to confirm the ion penetration, the degree of the ion penetration according to ion implantation energy of BF_2^+ and As^+ is analyzed by secondary ion mass spectroscopy (SIMS), respectively. Figure 2.5 illustrates the penetration of BF_2^+ and As^+ into the gate. In the case of BF_2^+, the implantation energy of 15 keV shows the high penetration of 10^{20} cm^{-3} up to 100 nm, corresponding to the gate thickness. However, in the case of As^+, the low infiltration of 10^{18} cm^{-3} up to 100 nm occurs by the implantation energy of 15 keV. Therefore, in the actual process, 15 keV is used for the BF_2^+ whereas the ion implantation is performed at 40 keV for the As^+.

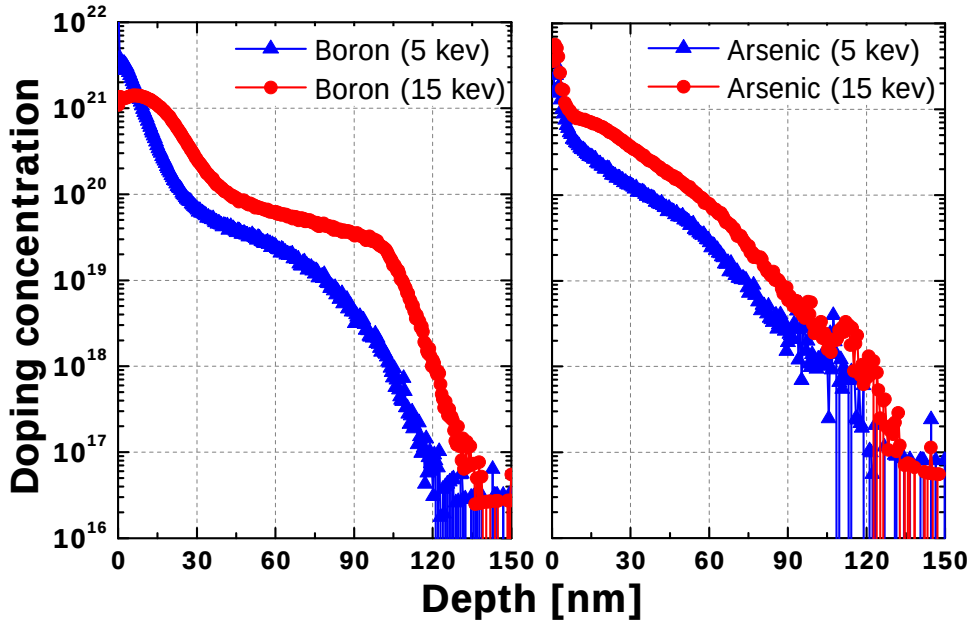

Fig. 2.5 Secondary ion mass spectroscopy (SIMS) analysis of ion penetration into gate by ion implantation energy.

The final key process is the formation of the sensing area. There is a possibility that the nanowire may be damaged if a large amount of etching is performed when the oxide film is etched to form the sensing region. However, if the amount of remaining oxide is too large, the nanowire cannot electrically detect the biomolecules. Therefore, it is important to select an appropriate etching time as similar to the poly-Si gate etching. Since the oxide film deposited as an ILD dielectric is considerably thick, the thickness of the remaining oxide film is continuously checked by repeating the oxide film etching and optical measurement of remaining oxide using Nanospec equipment.

Figure 2.6 shows the thickness of the remaining TEOS oxide film as a function of the oxide etch time. In Fig. 2.6, there is no data for the etching time of about 50 sec and 300 sec because the light interference occurs during the optical thickness measurement in the SOI wafer. Unlike silicon wafers, SOI wafers are made up of three layers of silicon-oxide-silicon. Figures 2.7(a) and (b) explain that the reflected light from each layer interferes with each other, preventing accurate thickness measurement and distorting data. Figure 2.7(c) shows the difference in TEOS oxide thickness measurements between general bulk silicon wafers and SOI wafers. The measurement results of the bulk silicon wafer and the SOI wafer are inconsistent at the oxide thicknesses of 200 nm and 400 nm. Although the actual process uses a SOI wafer, the sensing area can be stably etched by checking the thickness of the remaining oxide film in comparison with the bulk silicon wafer as shown in Fig 2.7(c).

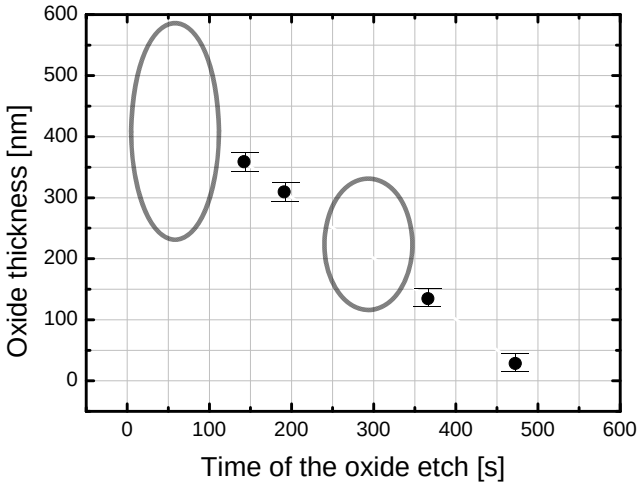

Fig. 2.6. Optical measuremets of the oxide thickness as a function of etching time.

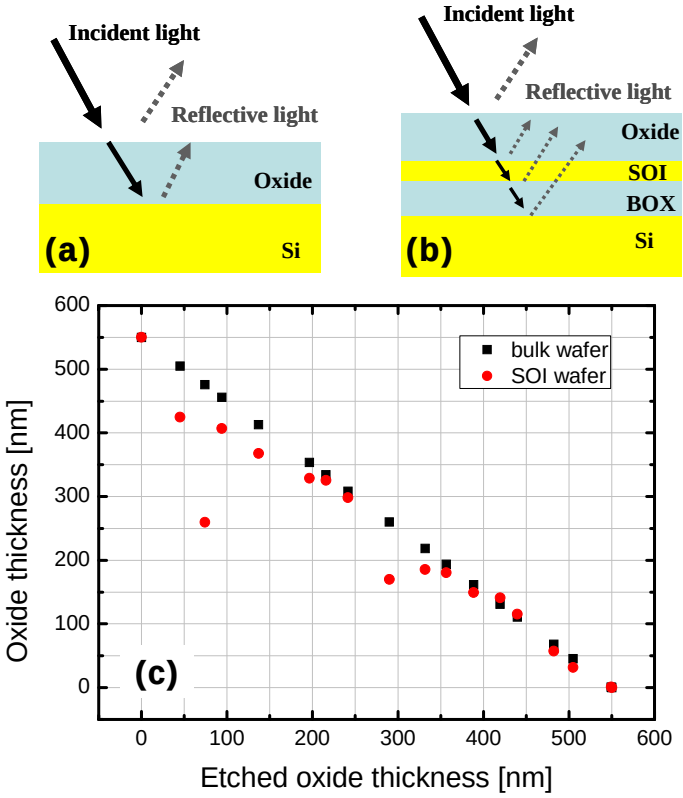

Fig. 2.7 Optical interference on (a) bulk silicon and (b) SOI wafers. (c) Comparsion of the measured oxide thickness in bulk silicon and SOI wafers.

2.3 Investigation of Fabricated Devices

Before the pH/biomolecules sensing experiments with the fabricated devices, the successful processing of the fabricated SiNW sensors is confirmed. Figure 2.8 is a photograph of a wafer and a single chip that have been processed. The fabricated SOI wafer is 6 inches in size and contains 81 single chips, 9 mm × 9 mm in size. A total of 11 masks is used in the wafer-level process, with 83 SiNW sensors integrated on each single chip. In order to use the micro-fluidic channel and to contact the SiNW with the solution, the SiNW sensor is in the center of a single chip and the pad to which the electrical input is applied is located on the outside of the chip.

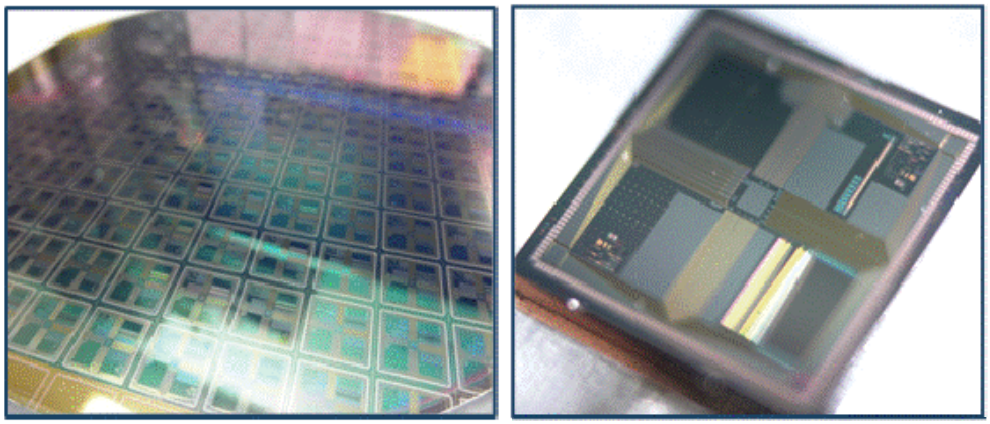

Fig. 2.8 Fabricated wafer and a single chip.

The successful formation of SiNWs to ensure a high surface-to-volume ratio directly related to the sensing performance of biosensors has been confirmed. Figure 2.9 is top view images of the sensor inside the chip by SEM. As can be seen in Fig. 2.10,

when the width of the nanowire is measured through an electron microscope, it is confirmed that more than 99% of the nanowires in the 6-inch wafer had the same actual line width as the designed line width. Thus, the proposed process flow is confirmed to be suitable for high-quality mass production. Figure 2.11 shows SEM and transmission electron microscope (TEM) cross-sectional images of the processed SiNW sensor. In the SEM cross-sectional image, it can be confirmed that the device is well fabricated as a whole and the sensing region is successfully etched. Additionally, through the nanowire TEM cross-section, it can be verified that the nanowire is well preserved during the sensing area etching process without damage as intended.

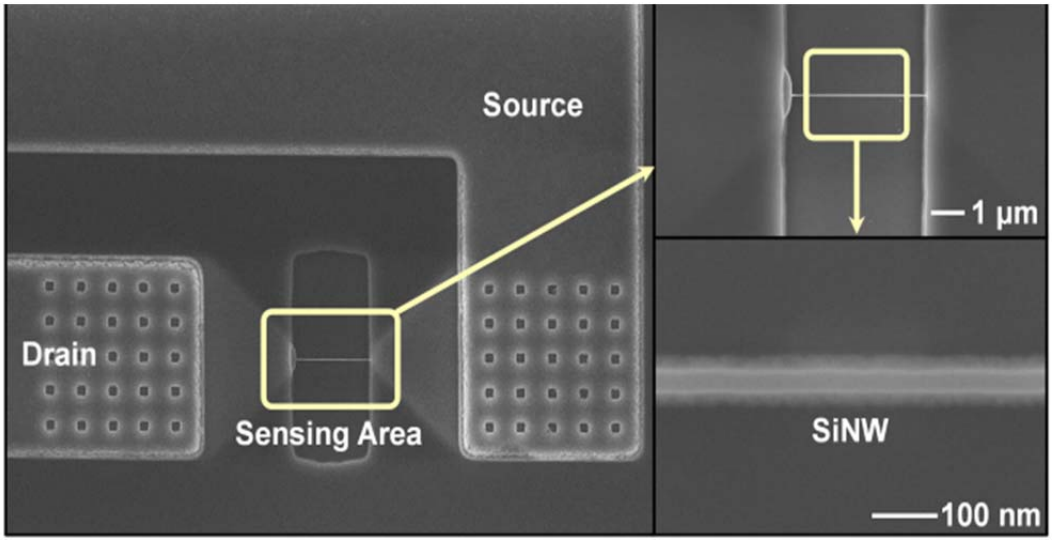

Fig. 2.9 Top view SEM images of the fabricated SiNW sensor.

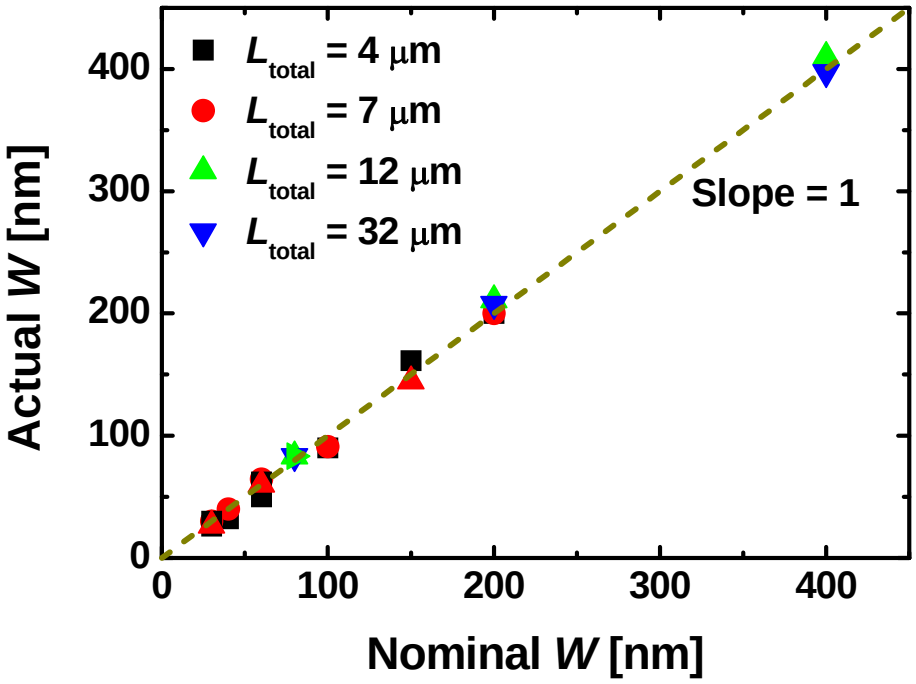

Fig. 2.10 Nominal *W* versus actual *W* of SiNWs integrated on the 6-inch SOI wafer.

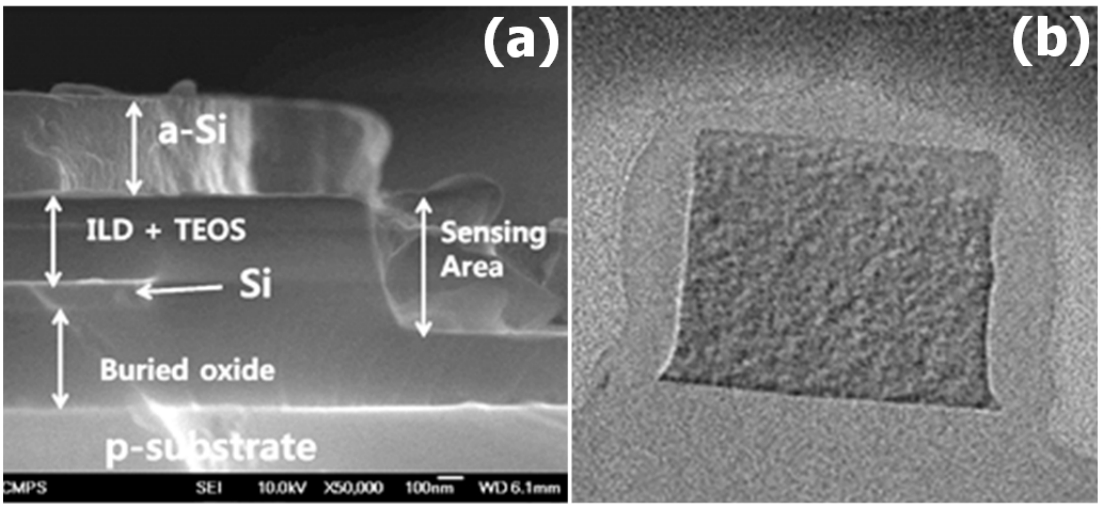

Fig. 2.11 (a) Cross-sectional SEM image of fabricated SiNW sensor. (b) Cross-sectional TEM image of SiNW.

2.4 Surface Treatement and Measurenment Setting

To have a linear change in total surface charge density as a function of pH, amine ($–NH_2$) functionalization is applied to the SiO_2 surface, which results in the linear response [31], [32]. Immobilization of $–NH_2$ on the thin oxide surface of the SiNW is prepared via the following three-step procedure. First, the device is treated by UV O_3 for 330 sec to introduce more hydroxyl (-OH) group on the SiO_2 surface than usual. Second, the device is functionalized with 1 % 3-aminopropyltriethoxysilane (APTES) in 95 % ethanol solution for 30 min. Last, it is dried in N_2 and heated on hotplate for 10 min at 120 °C. After 3 times of repeated rinsing with 95 % ethanol and dried in N_2, it is heated again at the same condition as above. As the result of the procedure, the $–NH_2$ surface is obtained on the thin oxide surface on the SiNW.

A polydimethylsiloxane (PDMS) fluidic channel is prepared for a fluidic transport of the analyte solution. First of all, PDMS master is fabricated on a 1-mm-thick 4-inch Si wafer in Fig. 2.12(a). The master is filled with a fully-stirred mixture of 40 g Sylgard-184 silicone elastomer and 4 g Sylgard-184 silicon elastomer curing agent and then it is baked at 80 °C for 3 hours. Then, the cured PDMS is taken off and cut to fit with the final chip dimensions around the channel. The volume of the cell is as follows: the size of the fluidic channel on the chip (9 mm × 9 mm) is approximately 4.6 mm × 3 mm × 200 μm (length×width×height). In order to construct a PDMS fluidic channel on the chip [Figs. 2.12 (b), (c) and (d)], they are exposed to UV O_3 for 330 sec and bonded together. Then, it is heated on a hotplate at 120 °C for 10 min. This procedure is

performed prior to the amino-functionalization because it is difficult to bond PDMS on the $-NH_2$ surface. The final measurement setup with tubing lines (inner diameter = 400 μm, outer diameter = 1.6 mm) on a probe station is shown in Fig. 2.12(d). A schematic diagram for the measurement setup using the PDMS fluidic channel is shown in Fig. 2.12(e).

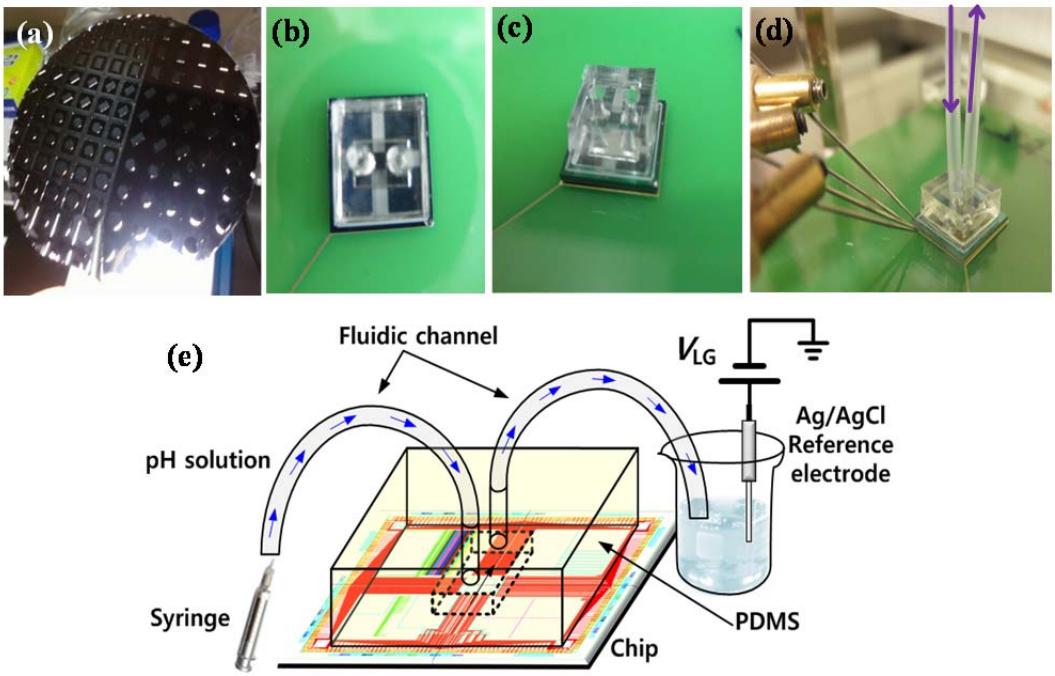

Fig. 2.12 (a) Fabricated PDMS channel master on 4-inch Si wafer. (b) Top view and (c) bird's eye view of PDMS channel attached to the fabricated chip. (d) Measurement setup with tube. (e) Schematic diagram of the measurement set-up.

The fabricated SiNW sensors have only the back-side gate (i.e. Si substrate) for measuremnets. However, The voltage applied to the the back-side gate causes the unstable measurement due to the fluctuation of the liquid potential [33]. For the reason,

the Ag/AgCl reference electrode is employed as a liquid-gate to control the reference electrical potential of electrolyte solution. In addition, potassium dihydrogen phosphate (KH_2PO_4) and potassium monohydrogen phosphate (K_2HPO_4) are used to control buffer solutions with HCl and KOH. The salt concentration used in this study are 0.1 M (pH 5~9). Disposable syringe is used to change the pH value of electrolyte solution. The electrical measurements are conducted with the semiconductor parameter analyzer (Agilent 4156C) after the flow of electrolyte solution is sufficiently stabilized.

Chapter 3

Co-integration of Sensors with Defect-free Sensing Material and V_{th}-tunable Devices

3.1 Concept of ISFET

As silicon technology is widely used for sensor development, the silicon devices are devised for the application to biosensors. One of the outstanding invention is ion sensitive field effect transistor (ISFET), proposed in 1970 by Bergveld [34, 35], which detect the hydrogen ions and produce electrical output. Due to their small size, rapid pH response and rugged solid-state construction, ISFETs exhibit a number of advantages over conventional pH-glass electrodes.

Since many biochemical reactions produce or release the hydrogen ions in the solution, it leads to changing concentration of the hydrogen ions. By detecting the

concentration, other reactions can also be probed. The popular example of ISFET application is non-optical DNA sequencing introduced by Ion Torrent of Life Technology [36]. The ISFETs can detect the DNA sequencing since the released protons from the ion sequencing produce a shift in the pH of the surrounding solutions. Since ISFET is the basic sensor in many biochemical sensors, many types of research of physical models provide well-understood operation mechanism. These are the reasons why our fabricated SiNW sensor operates as a pH detector.

Fig. 3. 1(a) shows the basic structure of ISFET measurement condition [37]. Since our devices are fabricated on a SOI wafer, the condition is like Fig. 3.1(b). The BOX and Si substrate act as a back gate insulator and a back gate, respectively. However, the measurement condition results in instability due to floating state of electrolyte, which is more dominant to nanowire channel [33]. In terms of theoretical background, the site-binding model is the most popular and well proven. A potential distribution and charges of Fig. 3.2 is the basis of physical models [37]. By using the site-binding model [37] and Poisson-Boltzmann equation, the surface potential (ψ_s) with the pH level at the interface between the sensing oxide and the electrolyte can be defined as follow:

$$\psi_s \ \alpha \ -2.303a\frac{kT}{q}(pH - pH_{pzc}) \tag{3.1}$$

where pH_{pzc} is the point of zero charges of the insulator, a is a constant dimensionless parameter such that the response of sensors varies linearly with pH of a solution [$0 \leq a$

≤1] [38]. That means the surface potential is proportional to the pH level. The common logarithmic change of the hydrogen concentration results in linear changes in the V_{th}.

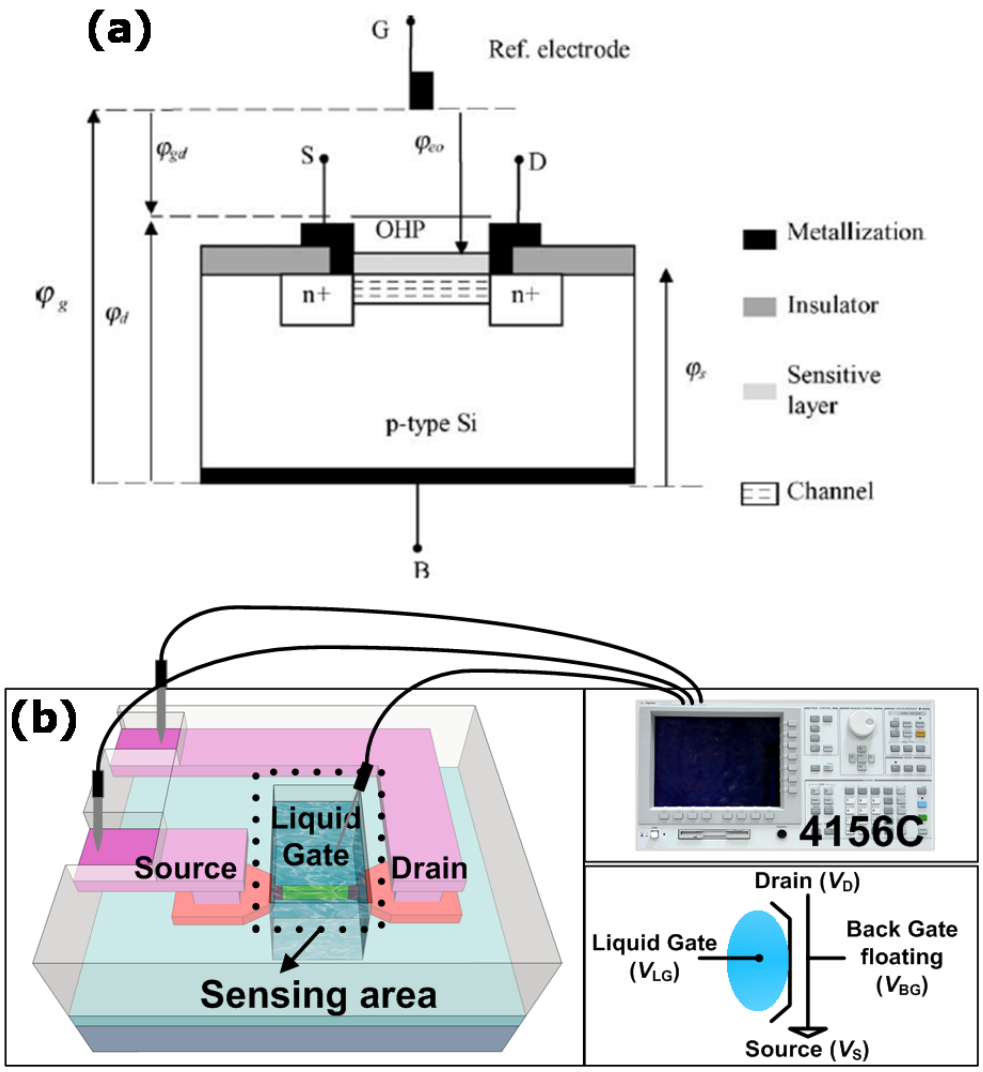

Fig. 3.1. (a) Typical measurement condition of bulk Si ISFET [36] and (b) that of fabricated sensor on a SOI wafer. The channel is isolated by BOX. OHP indicates the outer Helmholtz plane.

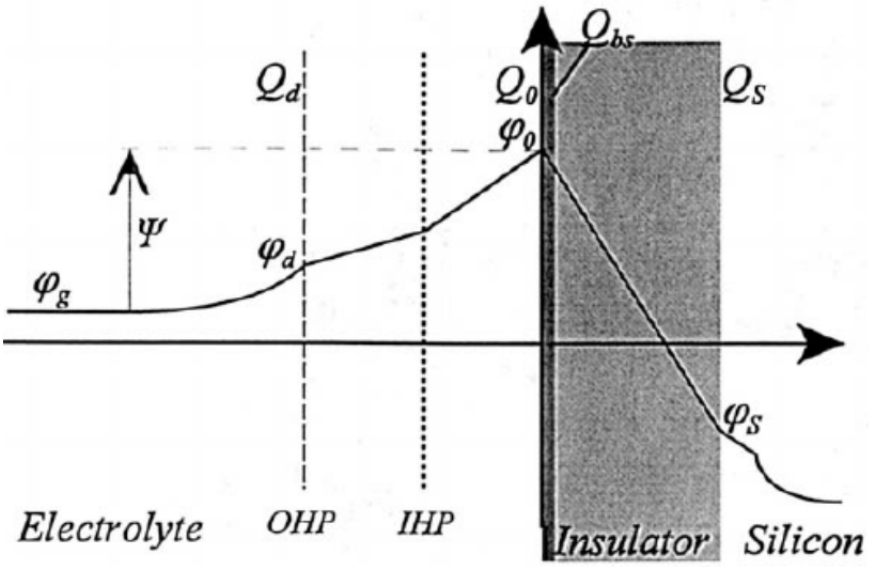

Fig. 3.2. Potential distribution and charges of an n-channel ISFET. OHP/ IHP indicate the outer/inner Helmholtz plane, respectively.

Considering the change of pH level, the surface potential changes more negatively when pH increases from Eq. (3.1). Therefore, n-type depletion mode SiNW becomes more depleted with the increase of pH and the p-type SiNW is more accumulated. The theoretical limit for the rate of change of surface potential with pH is predicted as

$$\frac{d\psi_s}{dpH} = -2.303a\frac{kT}{q} \tag{3.2}$$

The rate of the maximum change of the surface potential with pH is 60 mV/pH at room temperature according to Eq. (3.2), which is well-known as Nernst limit.

As the other application of the fabricated sensor, biomolecules can be detected as

similar to pH sensing. By attaching a receptor to sensing material on a channel that binds to a specific target biomolecule, various biomolecules besides hydrogen ions can be detected. According to the charge of the target biomolecule attached to the sensing material on the channel, the electric characteristics such as current, conductance, or resistance of the sensor are changed and thus the presence of the biomolecule can be detected electrically.

3.2 Problems in Sensing Area Etching Process

Dry etching and residual oxide thickness measurement are repeated to form the sensing region. Due to the limitations of thickness measurement, thicknesses of several tens of nanometers or less are not only unreliable, but over-etching is inevitable to expose the sides of the nanowire. The over-etching causes the sensing oxide or the nanowire surface to undergo plasma damage as shown in Fig. 3.3(a), resulting in the formation of a porous oxide film. The formation of a chemically unstable oxide film contributes greatly to the current drift phenomenon of the sensor.

In the case of excessive over-etching, the nanowires may be broken as shown in Fig. 3.3(b) due to the formation of micro-trenching by plasma crowding. Therefore, we have proposed a new fabrication process method that utilizes a top oxide-nitride-bottom oxide (ONO) insulator stacks to fundamentally eliminate plasma damage on the nanowire surface.

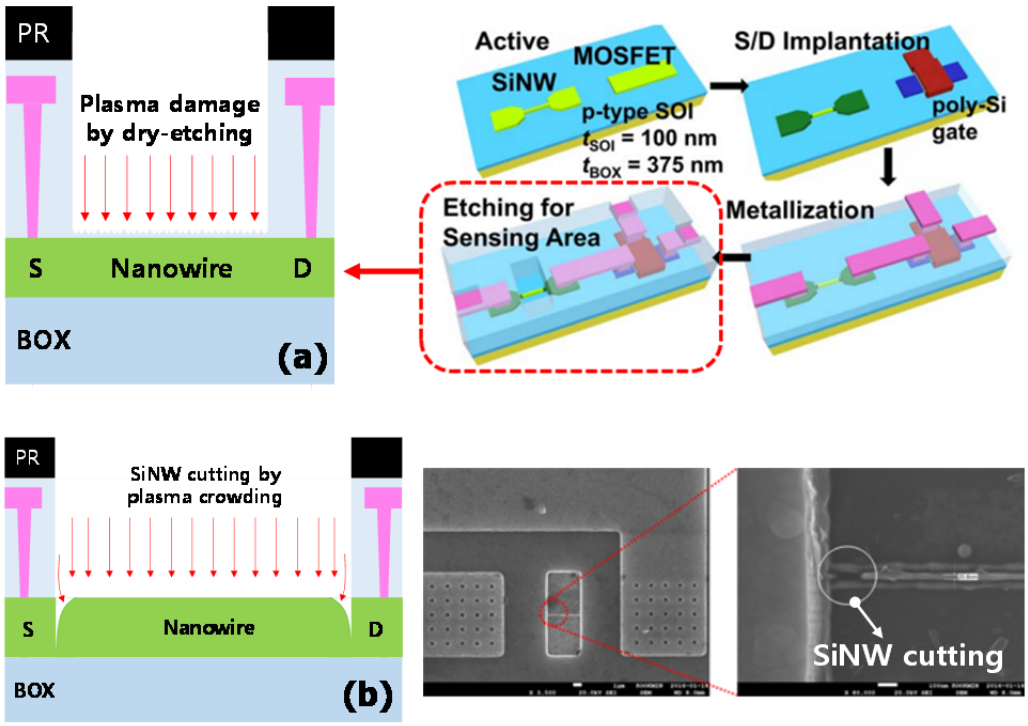

Fig. 3.3. (a) Plasma damage of silicon oxide and SiNW during dry-etching of sensing area. (b) SiNW breaking due to plasma crowding during dry-etching of sensing area. Top view SEM images of SiNW broken due to excessive over-etching.

3.3 Fabrication Process Using ONO Dielectric Stacks

In the process of forming the gate oxide film at the front-end-of-line (FEOL), a gate insulating film having a structure of ONO is deposited. The lower oxide layer is thermally oxidized, and the nitride layer and the upper oxide layer are deposited at a thickness of 4 nm/7 nm/10 nm using LPCVD. Then, when the sensing area is formed, the state shown in Fig. 3.4, 1 is obtained. As in the conventional sensing area formation, dry etching is performed until the remaining oxide film of several tens of nanometers

remains (Fig. 3.4, 2). The remaining ILD oxide layer and ONO top oxide layer are removed using a buffered HF solution (Fig. 3.4, 3). The nitride layer is selectively removed using a phosphoric acid solution (Fig 3.4, 4). Finally, only the chemically stable thermal oxide layer is left as the sensing oxide layer of the sensor, and the CMOS portion is completely protected from the dry/wet etching, so that the ONO gate insulating layer deposited in the FEOL is retained.

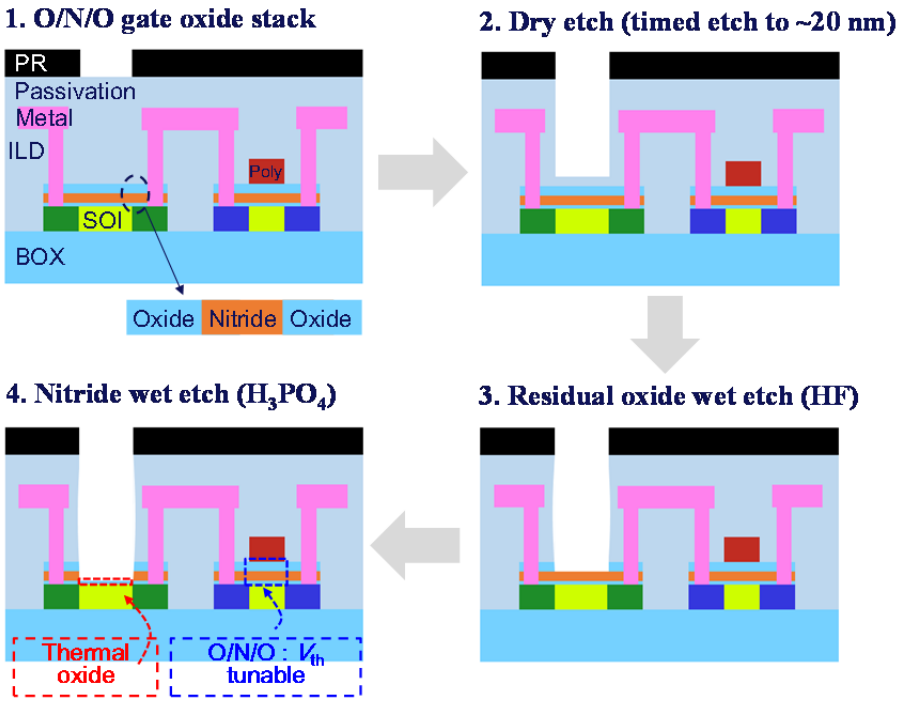

Fig. 3.4. Sensing area etching method using ONO gate dielectric (fabrication flow).

As a result, the plasma damage on the surface of the nanowire caused by the dry etching can be eliminated originally, and the drift phenomenon can be reduced by using

a stable thermal oxide film for sensing as compared with the conventional defective oxide film. Further, by using the ONO gate insulating film in the circuit devices, the V_{th} can be adjusted by storing the charge in the SiN. It is possible to solve the unevenness of the circuit operating voltage due to the distribution of the V_{th} occurring during the process.

In order to successfully form the sensing region using the above-mentioned wet etching, the SiN and the SiO_2 film must be selectively etched in phosphoric acid and hydrofluoric acid, respectively. That is, the SiO_2 and the SiN should not be substantially etched in H_3PO_4 acid and HF acid. To verify the wet-etching selectivity, the ONO (4 nm/7 nm/10 nm) layer is formed on the silicon substrate and wet etching is performed. In the case of the upper oxide film, the etching rate is about 3-4 nm per second in the HF solution. The etching is performed for 20 seconds considering sufficient over-etching. As shown in FIG. 3.5, the SiN is hardly removed by the HF solution. In the case of the SiN, the SiN has an etching rate of about 3-4 nm per minute in the H_3PO_4 solution. As a result of etching for 1 minute, 2 minutes, and 3 minutes, it is confirmed that the SiN is completely removed from 2 minutes as shown in FIG. 3.5.

The SiO_2 shows an etching rate of 0.135 nm per minute in the H_3PO_4 solution, and the selectivity ratio to the SiN is calculated to be about 23: 1. Also, the etching rate of the SiN in the HF solution is approximately 0.04 nm per second, and the selectivity ratio with respect to the SiO_2 is found to be extremely high, more than 100: 1. Through a series of experiments, it is confirmed that the SiO_2 and the SiN can be selectively etched

by wet etching. Based on the test results, we obtain the process conditions and applied them to actual device fabrication.

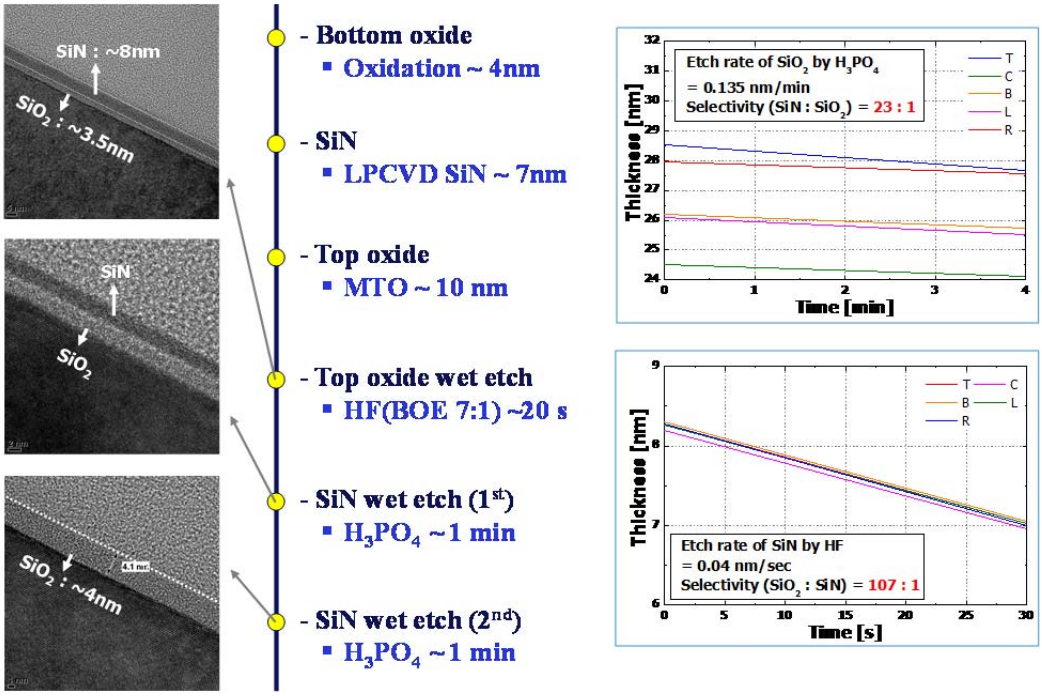

Fig. 3.5. Etching rate, selectivity ratio of SiO_2 and SiN in H_3PO_4 and HF.

To confirm the improvement of the device due to the proposed process, transmission electron microscopy (TEM) cross-sectional image of the fabricated device is confirmed. In the case of the device which forms the sensing region using the conventional dry etching, it can be confirmed that the surface of the SiNW is damaged as shown in FIG. 3.6(a), and it is observed that the amorphization is partially caused by the diffraction pattern. On the other hand, in the device in which sensing area is formed

by dry + wet etching using the newly proposed ONO gate insulating film, it is confirmed that there is no damage due to plasma in the channel as shown in FIG. 3.6(b) and that the single crystal is formed over the entire channel region by checking the diffraction pattern.

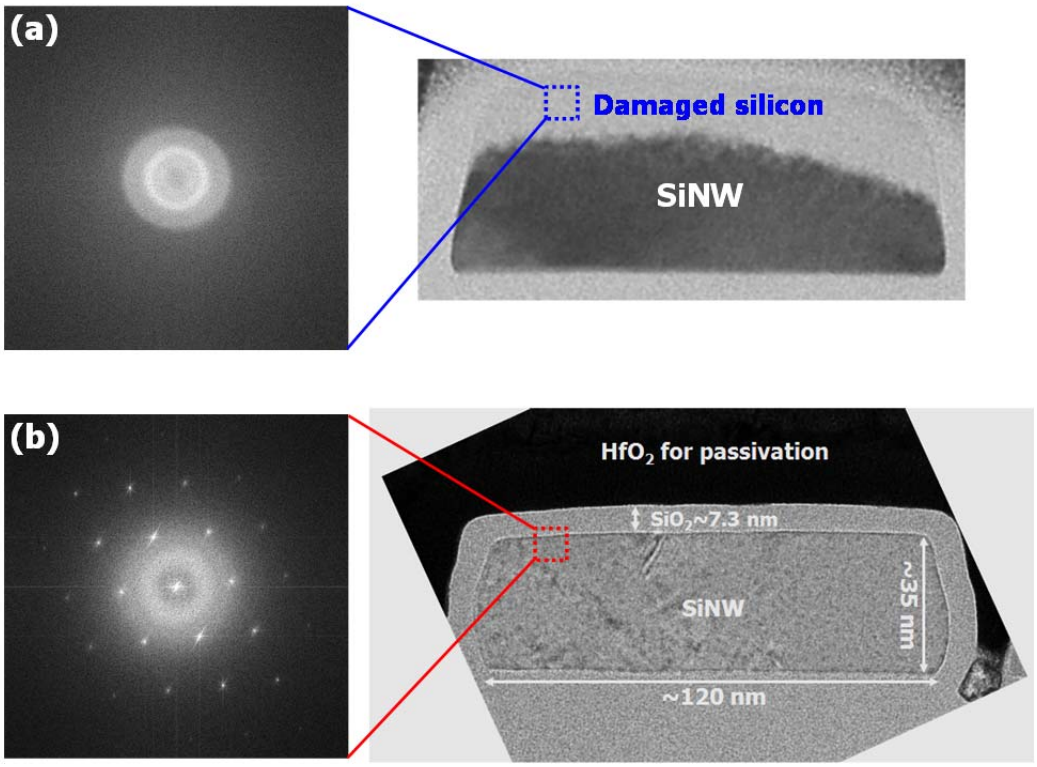

Fig. 3.6. TEM cross-sectional images and diffraction patterns of (a) the sensor fabricated by using a conventional dry etch and (b) the sensor fabricated by using the proposed dry + wet etching.

In the case of the devices in CMOS circuits, as described above, the ONO gate

insulating film can be preserved and can be utilized for adjusting the V_{th}. TEM cross-sectional images are investigated to confirm that the ONO layer of the intended thickness is formed. As shown in Fig. 3.7, it is confirmed that the ONO layer is deposited similar to the intended thickness (4 nm/7 nm/10 nm).

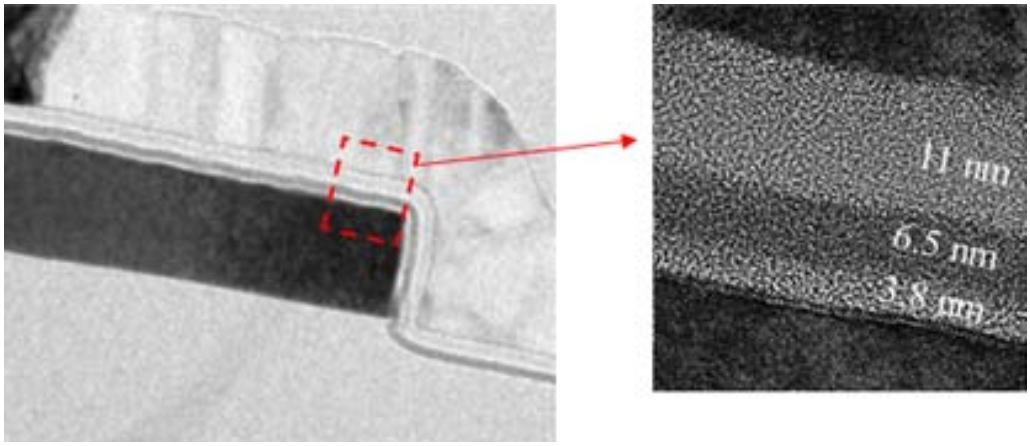

Fig. 3.7. TEM images of a gate stack of a circuit device.

Despite the successful formation of the sensing area by the proposed dry + wet etching, the metal lines are undesirably etched by the HF and the H_3PO_4 during the wet etching as shown in Fig. 3.8. This can be explained as follows: The PR covering the metal line is etched together without selectivity when the TEOS on the channel is dry-etched, and the PR on the sides of the metal lines is entirely consumed. In the subsequent wet etching, the passivation SiO_2 is removed by the HF and then the metal lines are etched by the penetration of the H_3PO_4.

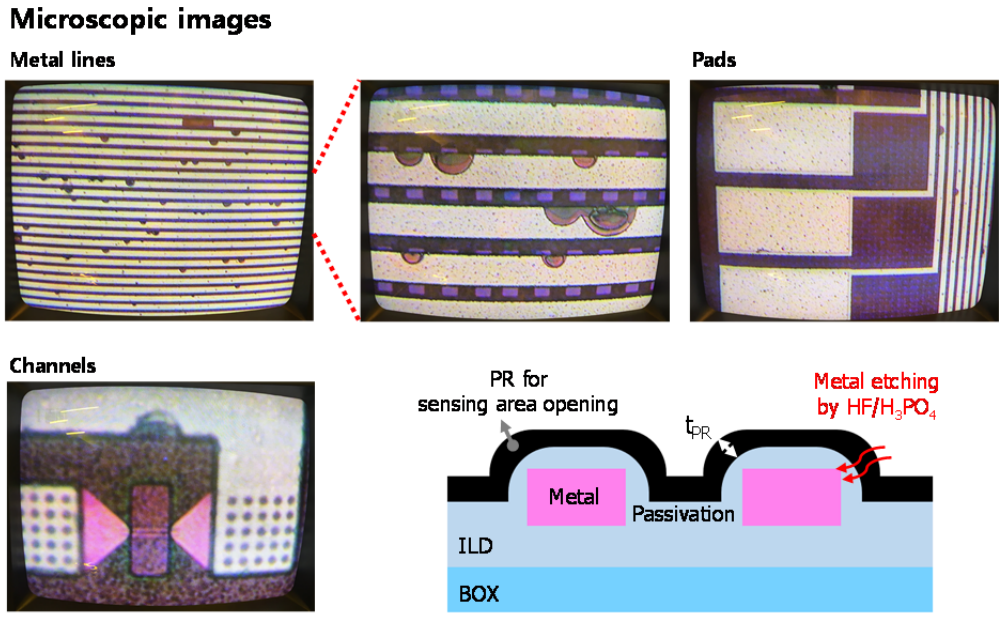

Fig. 3.8. Microscopic images of undesiably etched matal lines and metal line etching mechanism by the proposed dry + wet etching.

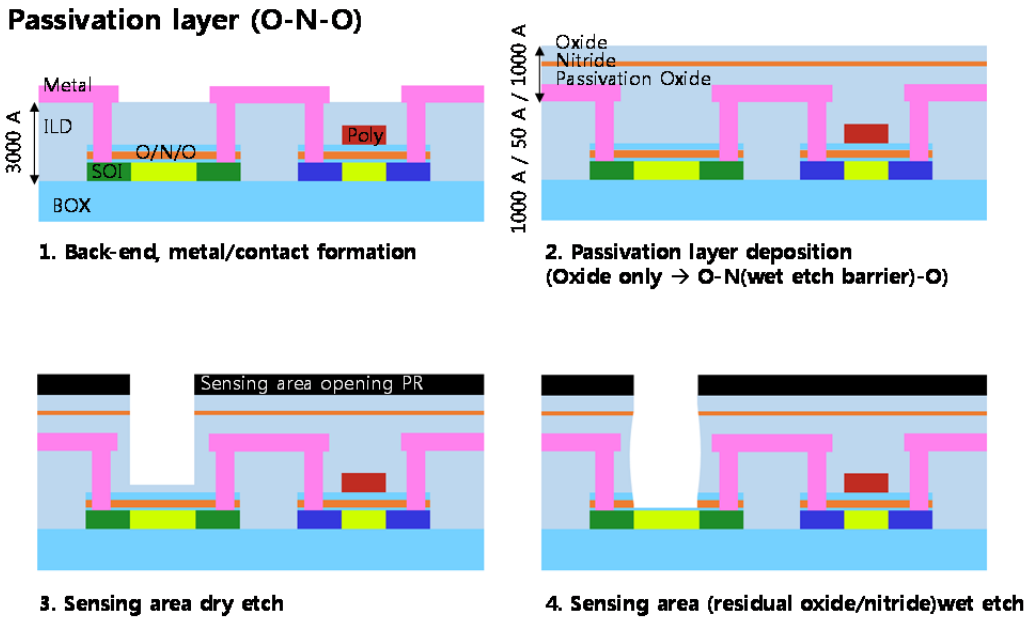

Fig. 3.9. Fabrication process flow using ONO as a passivation layer.

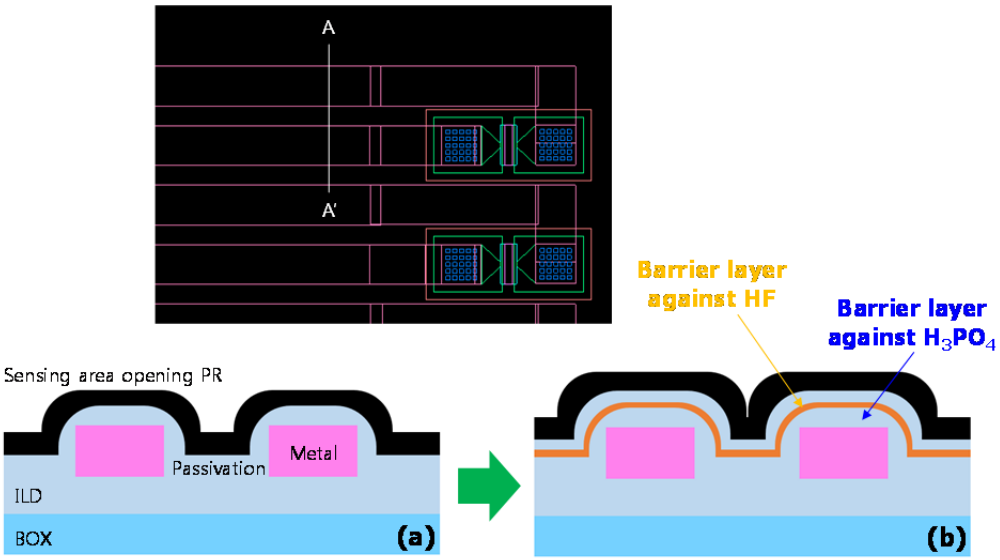

Fig. 3.10. Cross-sectional images of metal lines using (a) oxide and (b) ONO as a passivation layer.

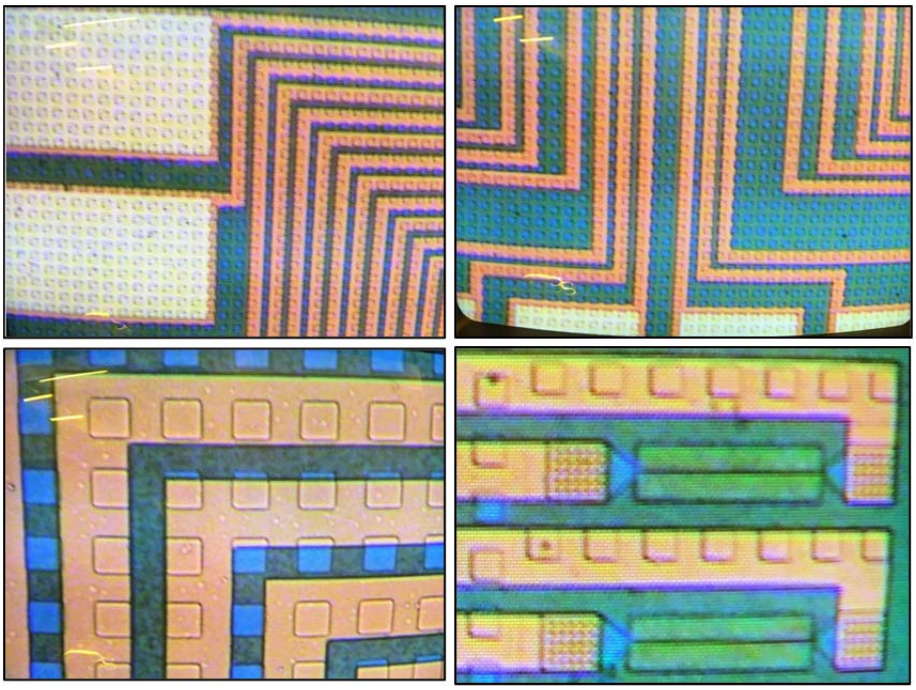

Fig. 3.11. Microscopic images of undamaged metal lines by using ONO dielectric stacks as a passivation layer.

To prevent the undesirable damage to metal lines, ONO layer is also used as a passivation layer on the metal lines. Although the PR on the sides of the metal lines is entirely consumed after finishing the sensing area dry etching of Fig. 3.9_3, Fig. 3.10(b) indicates that the penetration of the HF and the H_3PO_4 is blocked by the SiN and the bottom SiO_2, respectively. Consequently, the metal lines have no damage by using the ONO passivation layer after finishing the sensing area dry + wet etching, as can be seen in Fig. 3.11.

3.4 Electrical Characteristics of Devices Using ONO Stacks

The electrical characteristics of the sensor and the n-type MOSFET (nMOS)/p-type MOSFET (pMOS) in readout circuits are confirmed. As shown in Figs 3.12(b) and (c), the fabricated sensor performs stable pH sensing with V_{th} shift of 50 mV according to pH change. Fig. 3.12(d) demonstrates that the nMOS / PMOS show stable transfer characteristics.

The program and retention characteristics of nMOS with ONO gate insulator are investigated. In Fig. 3.13(a), the higher the gate voltage is applied to the nMOS, the higher the V_{th} is achievable by the program operation. In addition, Fig. 3.13(b) demonstrates that the electrons stored in the nitride layer by the program operation are well preserved at a high temperature of 110 °C for several hundreds of seconds without the V_{th} change.

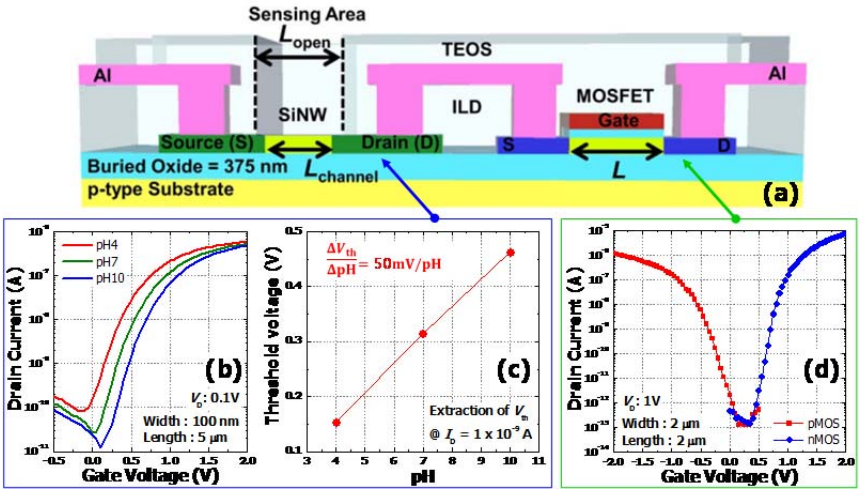

Fig. 3.12. (a) CSA Read-out circuit composed of one sensor and one nMOS. Changes of (b) transfer curves and (c) V_{th} as a function of pH. (d) Transfer characteristics of nMOS and pMOS in a read-out circuit.

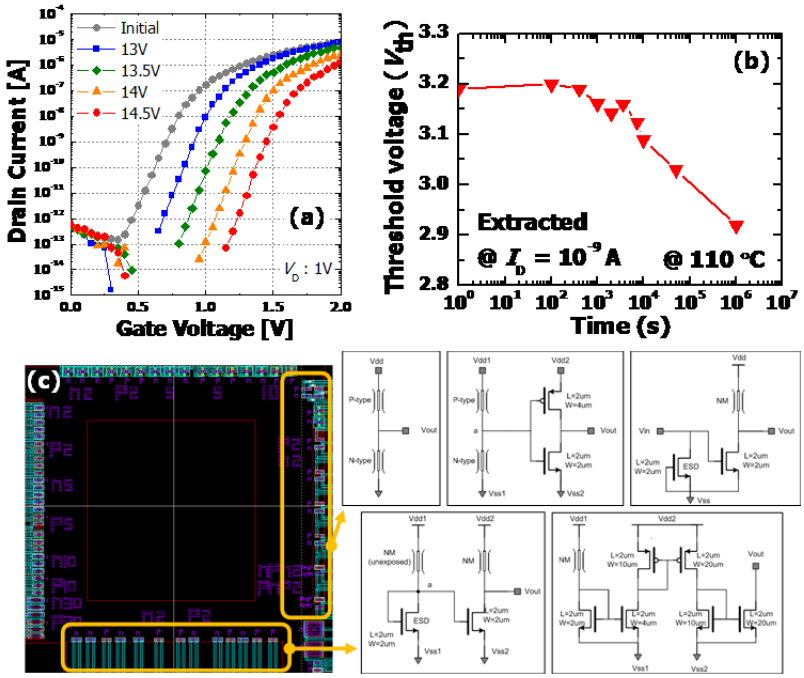

Fig. 3.13. (a) Program and (b) retention characteristics of an nMOS in a read-out circuit. (c) Various read-out circuits fabricated in a chip.

This stable adjustment of the V_{th} can be applied to various read-out circuits of Fig. 3.13(c). The V_{th} of the nMOS/pMOS in the various read-out circuits, which convert the current change (I_D change) by pH or biomolecules to the V_{out}, directly affects the V_{out} amplification. Therefore, the V_{th} of the nMOS/pMOS with the ONO gate insulator is fine-controlled through the program operation to maximize the V_{out} amplification.

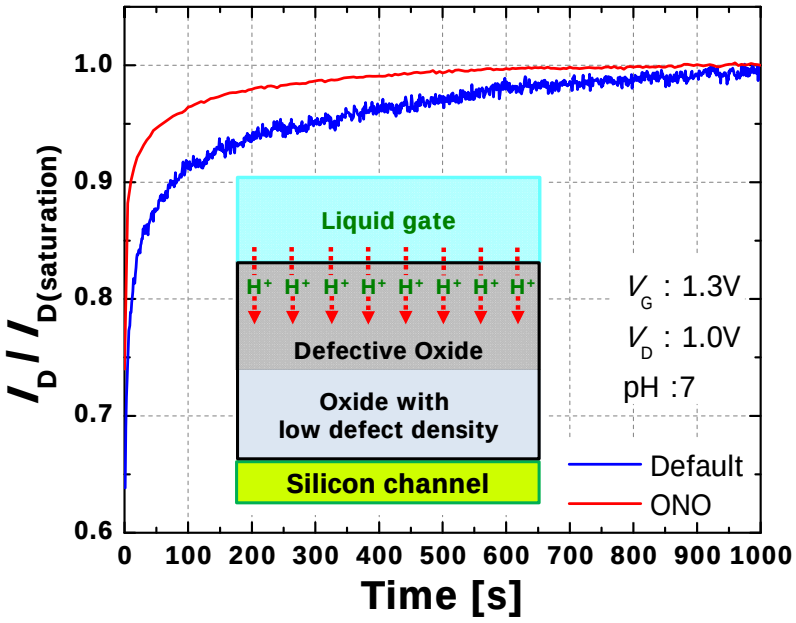

Fig. 3.14. Comparison of I_D-time characteristics of the sensor fabricated using the dry + wet etching process and the sensor fabricated using only dry etching process.

Figure 3.14 shows the comparison of I_D-time characteristics of the sensor fabricated using the proposed dry + wet etching process and the sensor fabricated using only dry etching process. When the sensing SiO_2 is chemically unstable (defective or

porous), the hydrogen ions penetrate into the defective SiO_2 as shown in the inset of FIG. 3.14 and the drift phenomenon (I_D is changed under a fixed V_{LG} as a function of measurement time and finally stabilized at a constant value after a long time) occurs in the consequence. If a chemically stable thermal SiO_2 is obtained through the dry + wet etching process after the ONO deposition, the penetration of hydrogen ions is significantly reduced because the thermal SiO_2 itself has few defects, and the I_D is stabilized to a predetermined value more quickly. Figure 3.14 also shows that the current noise caused by the movement of the ions during the I_D stabilization is significantly reduced.

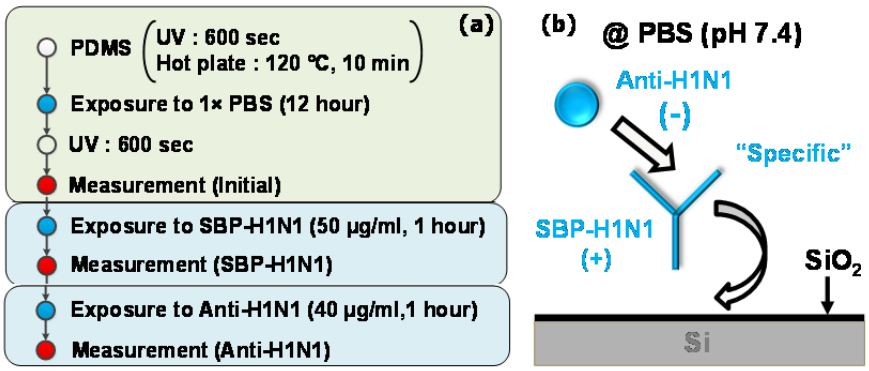

Fig. 3.16. (a) SBP-H1N1/Anti-H1N1 reaction sequence. (b) Specific binding of SBP-H1N1 to SiO_2 and selective reaction of Anti-H1N1 to SBP-H1N1.

To verify biomolecule detection, silica binding protein (SBP)-H1N1 and Anti-H1N1 are used as an antigen-antibody because the SBP-H1N1 is the protein reacted to the SiO2 (silica) and the Anti-H1N1 makes the specific binding to the SBP-H1N1,

which changes the V_{th} of the sensor as shown in Fig. 3.15(b) [39]. The SBP-H1N1/Anti-H1N1 reaction is conducted by the sequence of Fig. 3.15(a). Figure 3.16(a) shows a CSA circuit that converts the I_D change by the SBP-H1N1/Anti-H1N1 reaction to the V_{out}. Figure 3.16(b) shows that the V_{th} of the p-type MOSFET sensor fabricated by the proposed process has the ~150 mV V_{th} shift by the SBP-H1N1/Anti-H1N1 reaction. In Fig. 3.16(c), it is confirmed that the V_{th} of the nMOS with the ONO gate insulator is appropriately adjusted through the program operation. When the I_D change by the SBP-H1N1/Anti-H1N1 reaction is converted to the V_{out} using the CSA circuit, it is switched to the V_{out} change of ~ 400 mV as shown in Fig. 3.16(d).

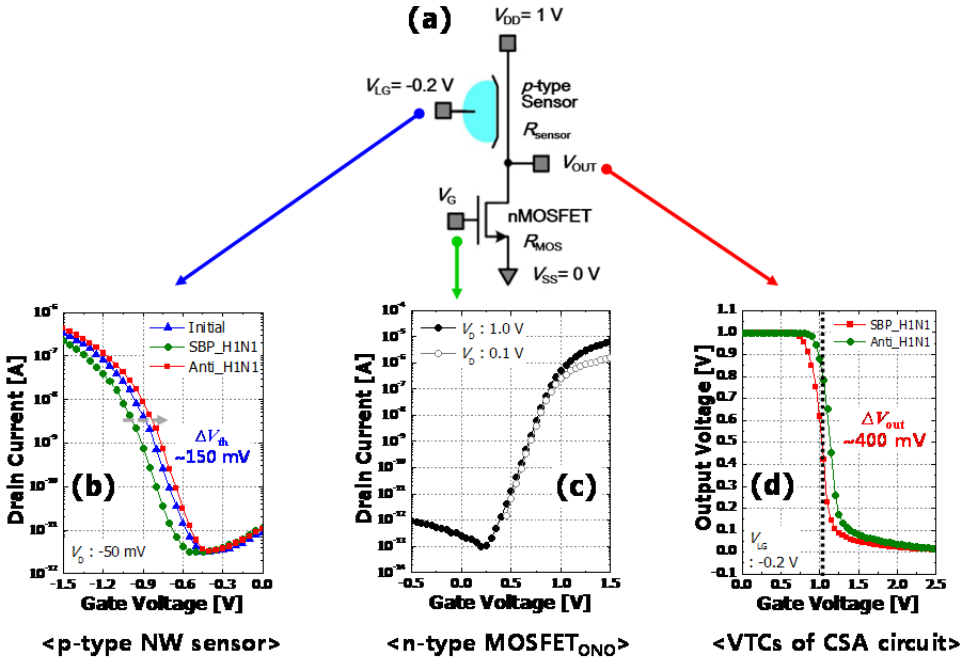

Fig. 3.16. (a) CSA circuit schematic. (b) Change of transfer curve of the p- type sensor according to SBP-H1N1/Anti-H1N1 reaction. (c) Transfer characteristics of the nMOS. (d) Voltage transfer characteristics (VTC) of the CSA circuit.

Chapter 4

TFET Sensor

4.1 Sensitivity Simulation

The device architecture and physical parameters of the Tunnel Field Effect Transistor (TFET) sensor used in this simulation study are shown in Fig. 4.1(a) and (b), respectively. The proposed device has a conventional p-i-n structure. The channel length and width of the device are 1 μm. The source and drain (S/D) regions are doped with 1×10^{20} cm^{-3} boron and arsenic, respectively, and channel doping concentration is 1×10^{15} cm^{-3}. In addition, we assume that Stern layer (or Helmholtz layer) can be considered as a dielectric layer with a few angstrom thickness [40]. Biomolecules are modeled as positive and negative charges on the gate oxide. The site-binding theory is used to model sensing mechanisms of target molecules with charges [41]. In order to analyze the electrical characteristics such as a sensitivity of the TFET sensor, mixed-mode

device and circuit simulations are performed by using Synopsys Sentaurus™ which is especially suitable for accurate tunneling current calculation because it automatically defines tunneling path and meshes on the basis of the valence-band gradient [42]-[44]. To reflect accurate tunneling currents, tunneling model is calibrated to experimental data (Planar TFT fabricated on SOI wafer) by using Kane's model [45].

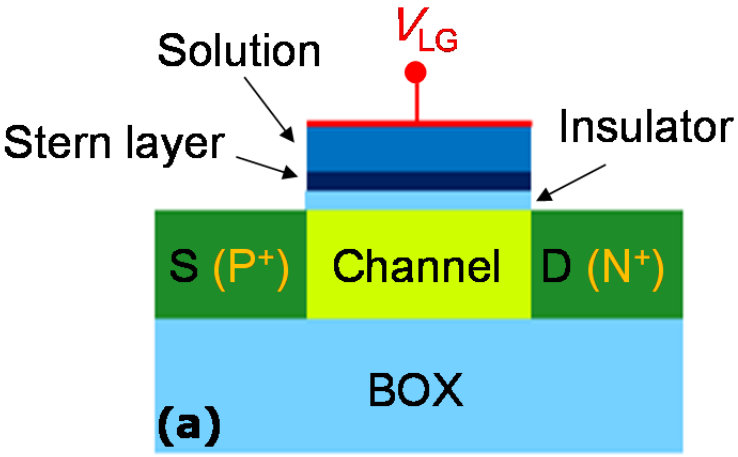

(b)

L_{ch}	1 μm
t_{ch}	40 nm
t_{ox}	1.5 nm
$N_{S/D}$	1 x 10^{20} cm^{-3}
N_{ch}	1 x 10^{15} cm^{-3}
t_{stern}	3 Å
t_{BOX}	375nm

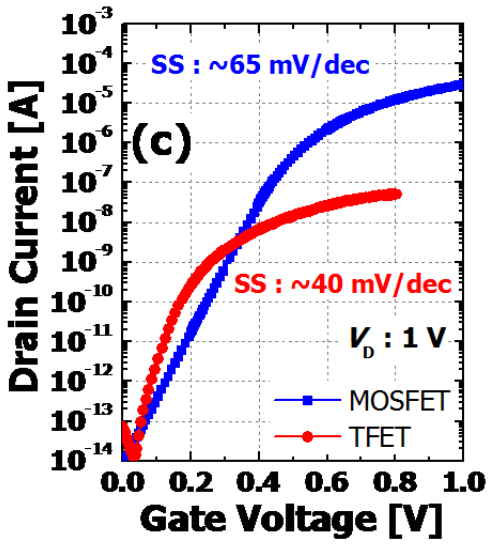

Fig. 4.1. (a) Device architecture and (b) physical parameters used in simulations. (c) Simulated tranfer characterisictics of MOSFET and TFET sensors.

Figure 4.1(c) shows that the basic simulated transfer curve of a biosensor based on a TFET has an SS smaller than that of a conventional MOSFET-based biosensor and a relatively low driving current. Unlike MOSFET sensors, the steeper SS of a TFET sensor is caused by the inherent mechanism by which current is generated by tunneling between source and channel rather than thermal carrier injection [46], and a low driving current is caused by a large tunneling resistance.

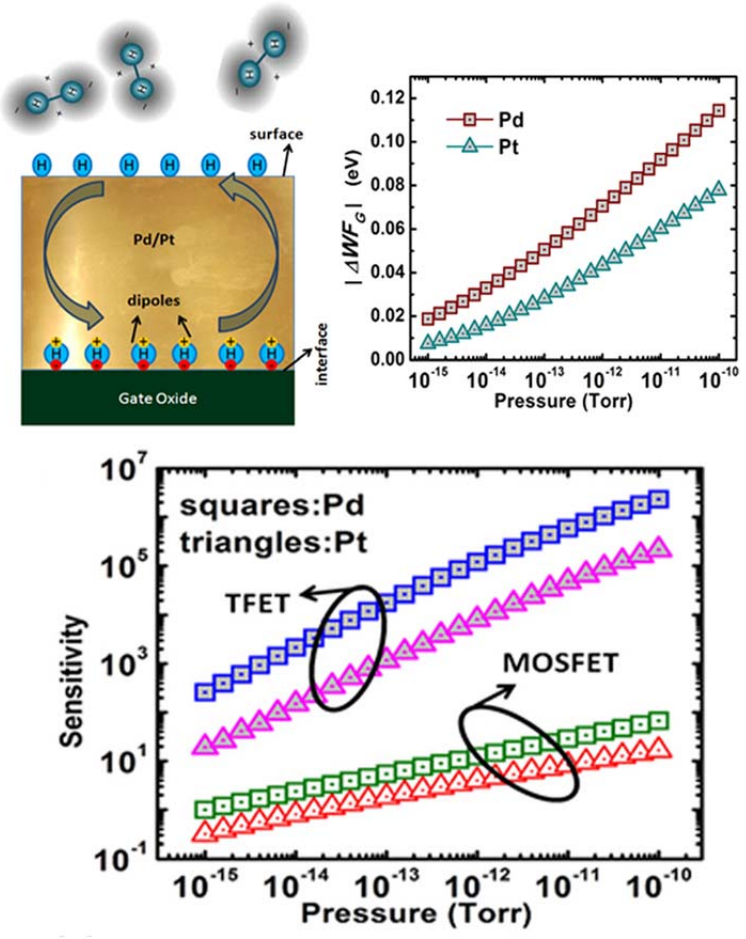

Fig. 4.2. Comparision of senstivities between MOFET and TFET sensor. All senstivities are extracted at SS region [47].

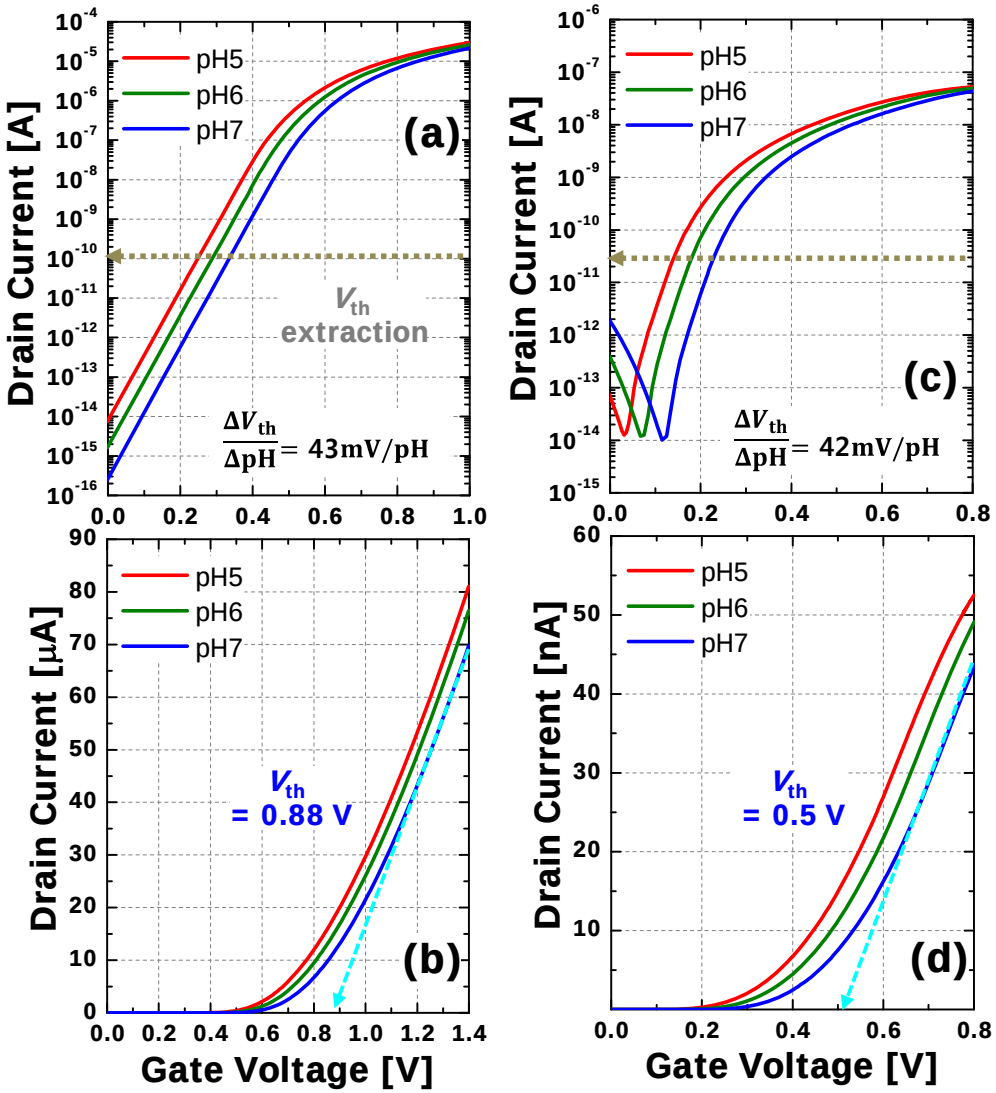

Fig. 4.3. Transfter curves according to pH of MOSFET sensor in (a) log scale and (b) linear scale. Those of TFET sensor in (c) log scale and (d) linear scale.

In the simulation, the change of pH is described by the charge density change of the stern layer [47] and the change of the transfer curve is examined as a function of pH level. As a result, Figs. 4.3(a) and (c) show that the V_{th} shift per the pH of the MOSFET and

TFET sensors are almost identical. However, the I_D sensitivity of the TFET sensor (I_D change per pH) is superior to that of the MOSFET sensor when the sensing is conducted below the V_{th} due to the steeper SS. When the sensing is performed in the SS region, high sensitivity can be obtained as reported in the previous study of Fig. 4.2 [48]. However, it is not desirable from a stable sensing point of view. Therefore, sensing at the point where I_D is saturated is essential for stable sensing.

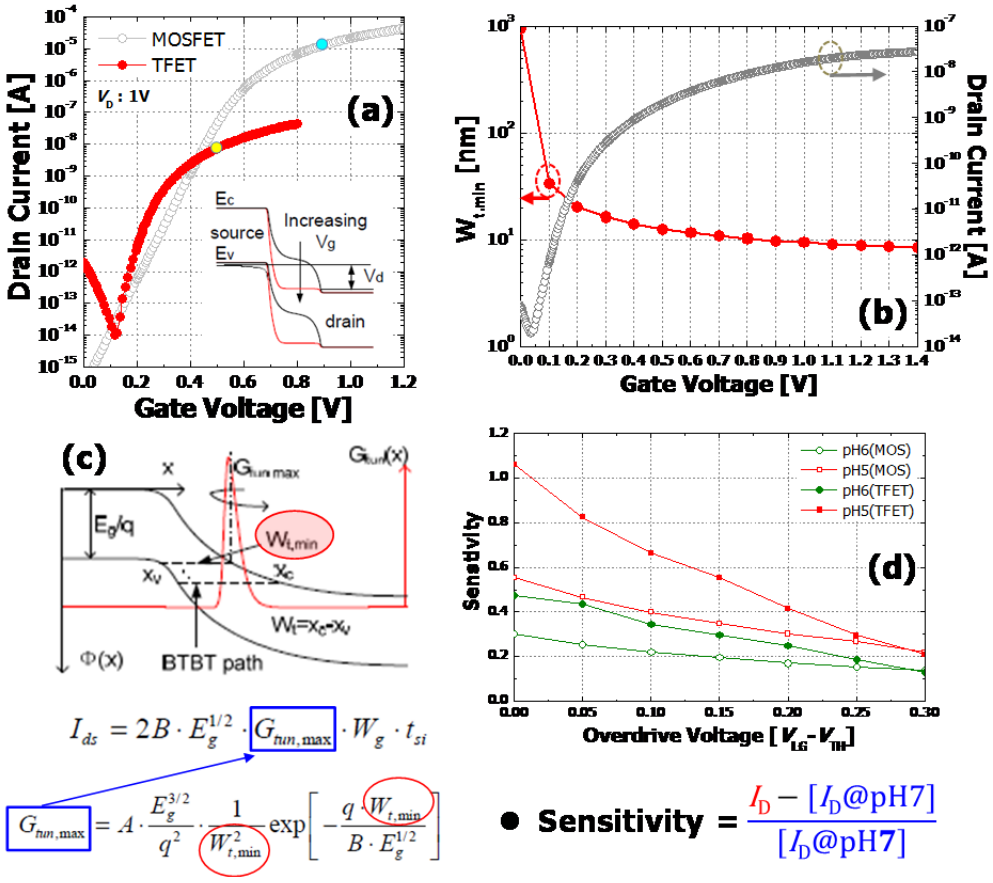

Fig. 4.4. (a) Transfer characterisitics of TFET and MOSFET. (b) Tunneling width as a function of V_G. (c) Relation between tunneling current and tunneling width. (d) Senstivity comparision between MOSFET and TFET sensors at saturated I_D range.

As the V_G increases, the TFET has two I_D saturation mechanisms, unlike a MOSFET in which a channel inversion layer is formed due to carrier injection from the source and thus the I_D saturates. First, at a relatively low V_G (First saturation), the increase in the tunneling current gets reduced as the decrease of the tunneling width between source and channel becomes saturated as shown in Fig. 4.3(b). When the V_G is further increased (Second saturation), carriers start to be injected from the drain and a channel inversion layer is formed similarly to the MOSFET, which leads to the second I_D saturation in the TFET. As shown in Fig. 4.3(d), at the point where the first I_D saturation of the TFET occurs, the increase of the I_D with the change of the pH is larger than that of the MOSFET. It means that the TFET can have more excellent sensitivity than MOSFET. However, after the I_D saturation by the carrier injection from the drain (namely, second I_D saturation), there is almost no difference in I_D sensitivity according to the pH change because the I_D saturation occurs by the same mechanism in both the MOSFET and the TFET. Consequently, the TFET sensor can have the higher I_D sensitivity compared to the MOSFET sensor, even though stable sensing is possible in the saturated I_D region until the second I_D saturation occurs from the point where the I_D is first-saturated.

4.2 Measurements of Fabricated TFET Sensor

The diode current measurements are performed to verify that the source (p^+),

channel (p^-), and drain (n^+) junctions of the TFET are formed as desired. As shown in Fig. 4.5, when the source is grounded and the drain voltage is swept while the liquid gate is floating, the forward diode current is formed in the TFET having the p-i-n junction, unlike the MOSFET.

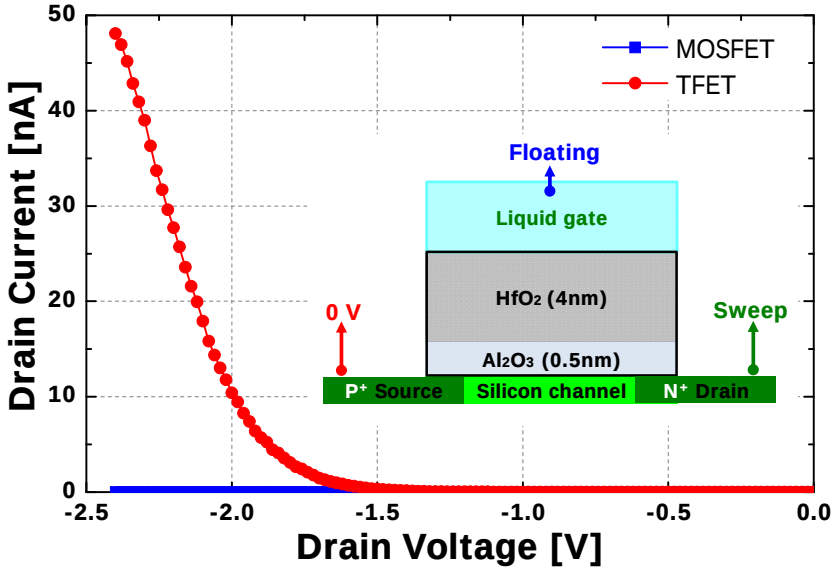

Fig. 4.5. Result of diode current measurement of TFET sensor.

I_D-V_G characteristics are examined. As expected from the simulation, Fig. 4.6(a) shows that the TFET sensor has superior SS characteristics to the MOSFET sensor. The graph of SS according to the I_D indicates that SS is less than 60 mV/Dec (SS limitation of MOSFETs at room temperature) in 3-order or more current range as can be seen in Fig. 4.6(b). Furthermore, the TFET sensor has a higher driving current than the previously reported TFETs and even does not show a significant difference from the

MOSFET sensor integrated into the same chip. This can be understood that the sensing area, which is the portion where the V_G is applied through the electrolyte, is overlapped with source and drain over a large area (about 0.5 um). Figure 4.6(c) explains that the inter-band tunneling occurs vertically at the overlap of the gate and the source, which is larger than that of the conventional TFETs because the vertical tunneling area is considerably larger than the horizontal one.

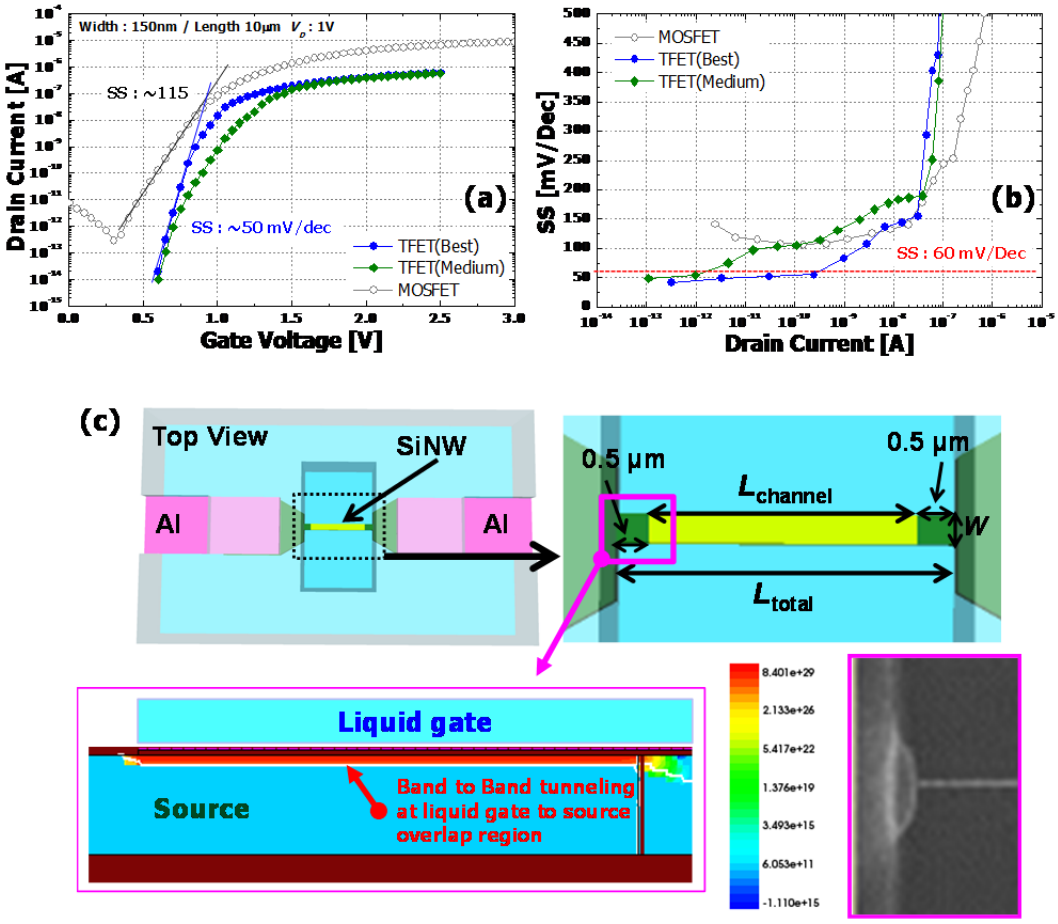

Fig. 4.6. (a) Transfer characterisitics of fabricated MOSFET and TFET sensors. (b) SS according to I_D. (c) Analysis on large tunneling current of fabricated TFET sensor.

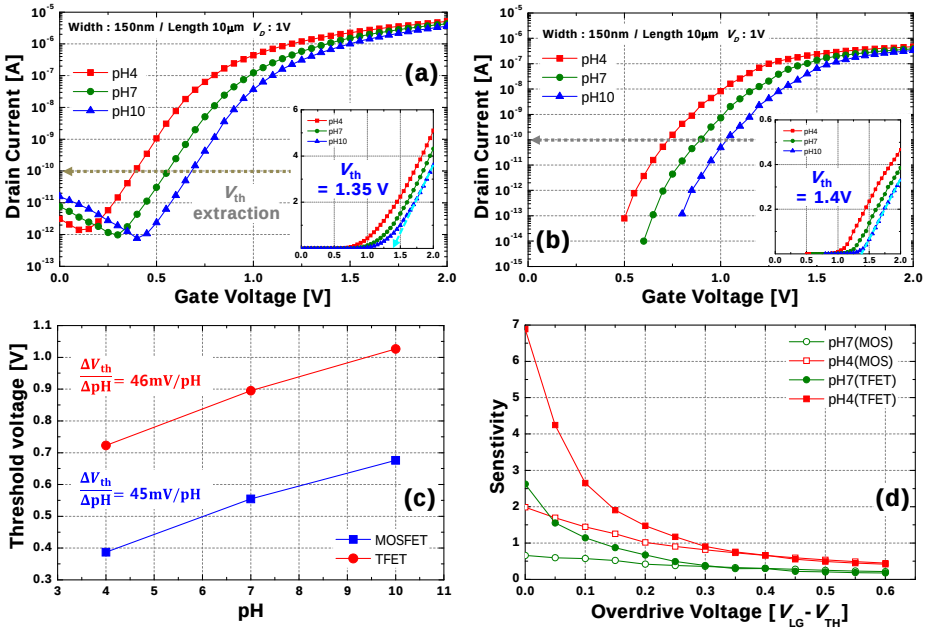

Fig. 4.7. Transfer characteristics of (a) MOSFET and (b) TFET sensors with pH variation. (c) Variation of V_{th} according to pH and (d) Sensitivity to overdrive voltage.

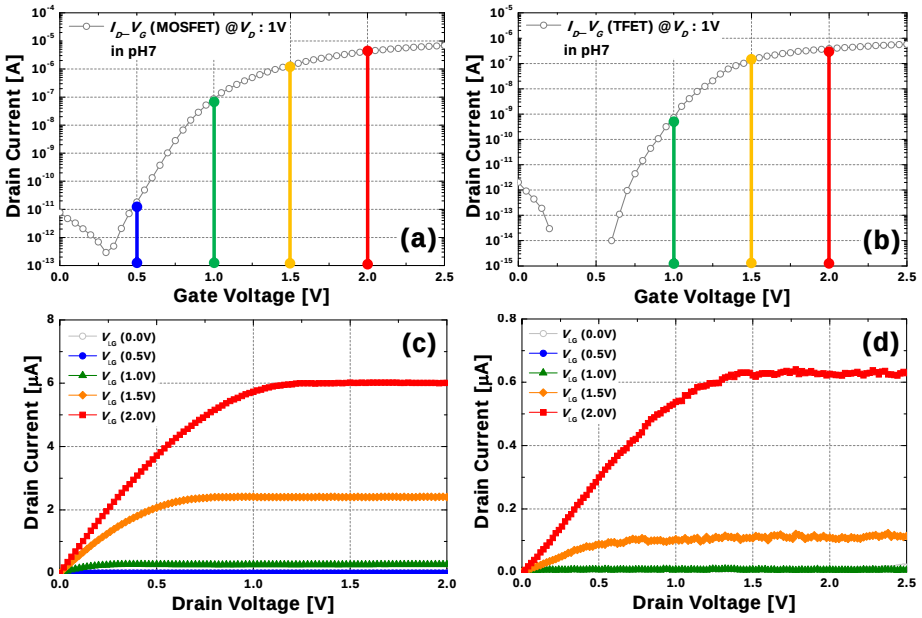

Fig. 4.8. (a) Transfer and (c) output characteristics of MOSFET sensor. (b) Transfer and (d) output characteristics of TFET sensor.

The change of I_D-V_G characteristics according to pH variation are compared between fabricated MOSFET and TFET sensors. As can be seen in the above-mentioned simulation results, the TFET sensor has superior SS and the V_{th} changes by pH variation are similar to those of the MOSFET sensor. Through the measurements of the fabricated devices, it is confirmed that the current sensitivity of the TFET sensor is more excellent when the overdrive voltage is small (the first current saturation region of the TFET), and there is no difference in sensitivity between the MOSFET and TFET sensors from the second current saturation region of the TFET.

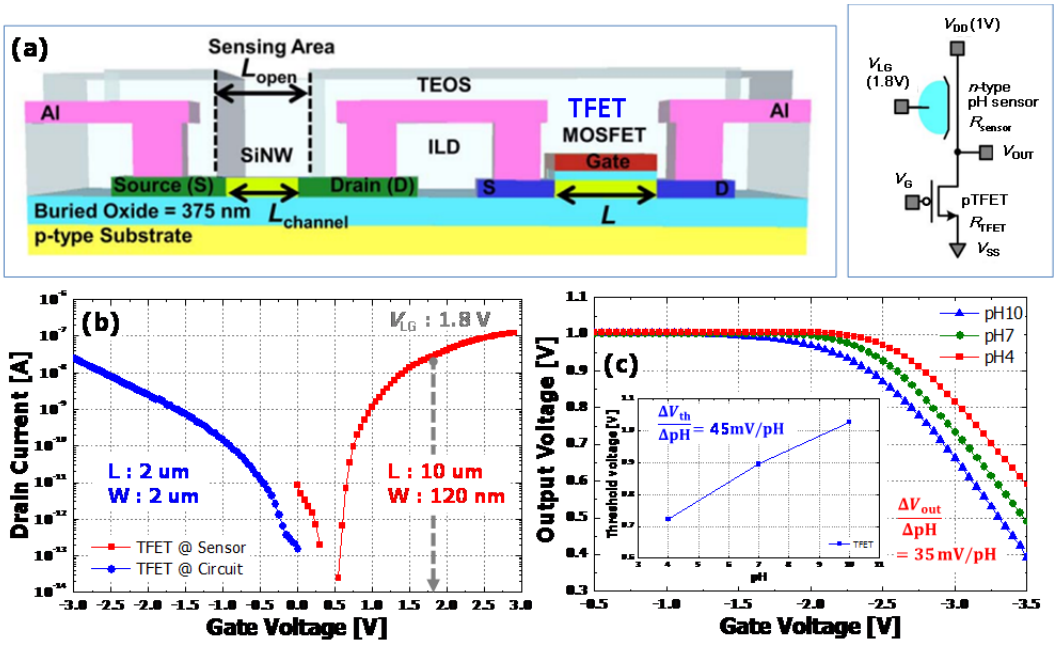

Fig. 4.9. (a) Corss-sectional structure and schemetic diagram of CSA circuit. (b) Transfer characteristics of p-type MOSFET and n-type sensor in CSA circuit. (c) V_{th} shift per pH and VTCs of TFET circuit

Before investigating the read-out circuit operation in Fig. 4.9(a), which consists of

a sensor and a TFET/MOSFET device, we measure the output characteristics (I_D-V_D) to determine the operating region of the MOSFET/TFET sensor. As shown in Fig. 4.8(d), the TFET sensor shows super-linear characteristics due to the relatively large tunneling resistance at a low drain voltage (V_D).

We have confirmed the operation of the simplest CSA among the various circuit configurations where the TFET sensor with exposed SiNWs and the TFET devices with polysilicon gates are integrated. The circuit configuration is a voltage read-out circuit in which the n-type TFET sensor and the p-type TFET device are connected in series as shown in the schematic diagram of Fig. 4.9(a), and the I_D change of the sensor according to the pH change is converted into the V_{out} change. The transfer characteristics of the TFET sensor and the TFET device are examined to confirm the performance as a single device and a component of CSA circuit. It can be seen that the sensor having a structure in which the source overlaps with the liquid gate has a larger driving current than the TFET device even though the channel width is small. The CSA operation is confirmed by sweeping the V_G of the TFET device at V_{LG} = 1.8 V and V_{DD} = 1 V of the sensor. As shown in Fig. 4.9(c), as the pH increases, the resistance of the sensor becomes larger and the V_{out} becomes smaller at the fixed V_G of the TFET device by the voltage division of the two devices. As a result, the sensitivity is measured at 35 mV per pH.

Chapter 5

Multiplexed Sensing

5.1 Concept of Multiplexed Sensing

The multiplexed sensor is believed to be especially important for the robust diagnosis of complex disease such as cancers in human blood and could further facilitate early detection [49]. In the previously reported works, different receptors should be separately immobilized on an individual device to allow selective multiplexed detection [49], [50]. It has been developed that integrated nanowire arrays in which distinct nanowires and surface receptors can be incorporated as individual device elements as shown in Fig. 5.1(a). However, the proposed method has a drawback that too many sensors (namely, chip area) are used for multiplexed -sensing.

In this work, two different biomolecules can be detected in one biosensor independently by forming different types of sensing materials on the source and drain regions of the channel and by reacting receptor molecules (Receptor A and B) which are bound with two different target biomolecules (Target A and B) to each sensing material, as can be seen in Fig. 5.1(b).

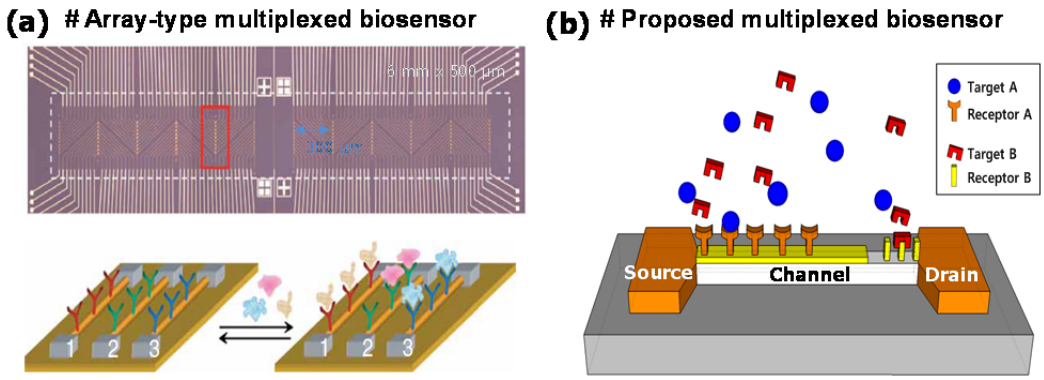

Fig. 5.1. Comparision of (a) previously reported multiplexed-sensing [48] and (b) proposed multiplexed-sensing.

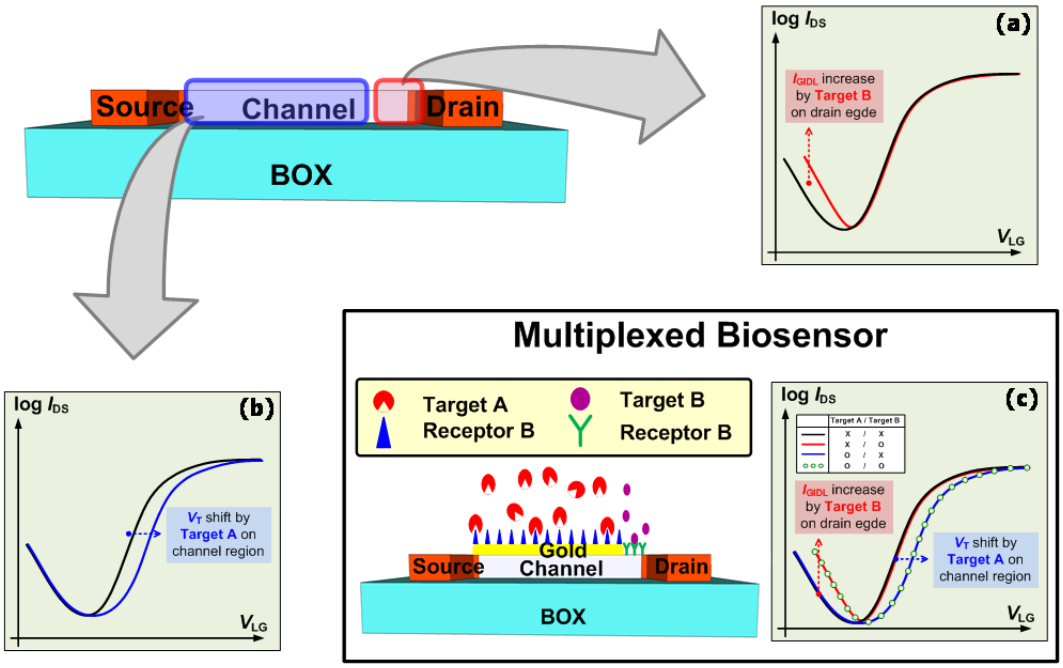

Fig. 5.2. Concept of multiplexed sensing using SiNW MOSFET sensor. (a) GIDL change by receptor B and target B attacted to drain edge. (b) V_{th} shift by receptor A and target A attacted to remaining part except for drain edge. (c) Multiplexed sensing of target A and B in one sensor.

5.2 Multiplexed Sensing in MOSFET Sensor

As shown in Fig. 5.2, two different biomolecules can be independently detected in a single device by using the gate induced drain leakage (GIDL) phenomenon occurring at a specific V_G of a MOSFET. When one receptor (Receptor B) attached to the drain edge reacts with one biomolecule (Target B), a change in GIDL is observed at a V_G region where GIDL occurs, whereas a V_{th} is shifted when the other receptor (Receptor A) attached to the remaining part except for the drain edge reacts with the other biomolecule (Target A).

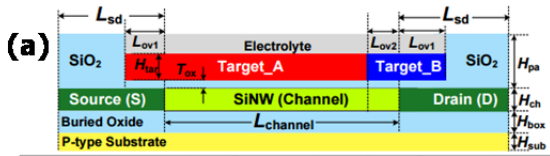

Parameter	Value	Unit	Parameter	Value	Unit	Parameter	Value	Unit
Q_{target}	$\pm 5.8 \times 10^{19}$	cm^{-3}	N_{ch}	10^{17}	cm^{-3}	$N_{S/D}$	10^{20}	cm^{-3}
ε_{target}	$78.5\varepsilon_0$	F/m	H_{tar}	5	nm	H_{ch}	12	nm
$L_{channel}$	1	μm	L_{sd}	0.2	μm	T_{ox}	2	nm
H_{pa}	0.1	μm	L_{ov1}	100	nm	L_{ov2}	40	nm

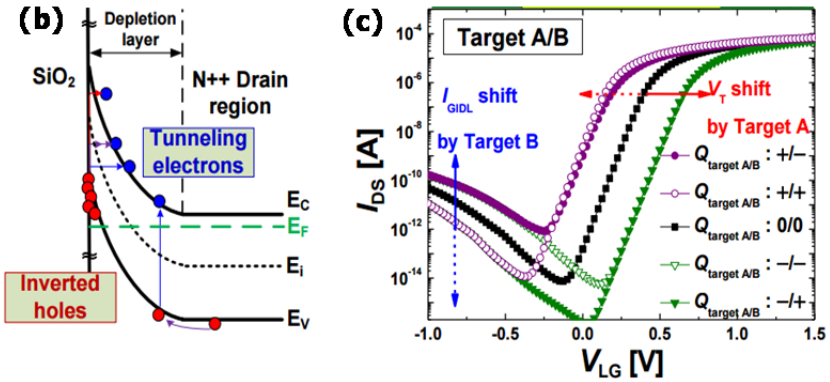

Fig. 5.3. (a) Schematic diagram of 2-D TCAD simulation to verify the operation of the proposed multiplexed biosensor. (b) Energy band diagram of drain edge overlapped with liquid gate. (c) Transfer characteristics of the multiplexed sensor according to the location and/or the type of charge of two different target molecules.

Before the experiment, the effects of the multiplexed sensing are verified by using 2-D TCAD simulations. Figure 5.3(a) shows the simulated device structure where the source/drain is overlapped with the liquid gate and the detailed device parameters used in the simulations. To mimic two different biomolecules with a charge in the simulations, the charge of Target A is attached to the remaining part except for the drain edge and the charge of Target B is added to the drain edge. Then, the I_D-V_G curves of the MOSFET sensor are compared according to the polarity of each charge. As a result, Figure 5.3(c) demonstrates that only the V_{th} is changed without changing the GIDL current when the polarity of Target A is changed, whereas only the GIDL current is changed without changing the V_{th} when the polarity of Target B is changed. This phenomenon can be explained that the charge of Target A affects only the V_{th} shift because a V_{th} shift is determined by an energy barrier between source and channel, while the GIDL is changed only by the charge of Target B since GIDL is generated by band-to-band tunneling (BTBT) current at the overlapped region between liquid gate and drain as can be seen in Fig. 5.3(b). Through the TCAD simulations, each device/structure parameter is optimized to obtain stable conditions for interference-free multiplexed sensing and the determined parameters are applied to the multiplexed sensing experiments.

5.3 Fabrication Process and Biomolecules Reaction

In order to selectively attach two different receptors, a specific substance must be

applied to the entire surface of the channel except for the drain edge region. In this experiment, gold is deposited and patterned to attach a gold-responsive receptor [Gold binding protein (GBP)-AI]. Figure 5.4(a) shows the gold formation process at the reaming channel part except for the drain edge region. First, PR is patterned and remained at the drain edge (the part where the gold is not covered). Then, the PR and gold are removed through the lift-off process. As a result, the gold is selectively patterned only at the entire surface except for the drain edge. Figure 5.4(b) shows the microscopic top-view image of the SiNW sensor partially covered with the gold formed by the proposed lift-off process.

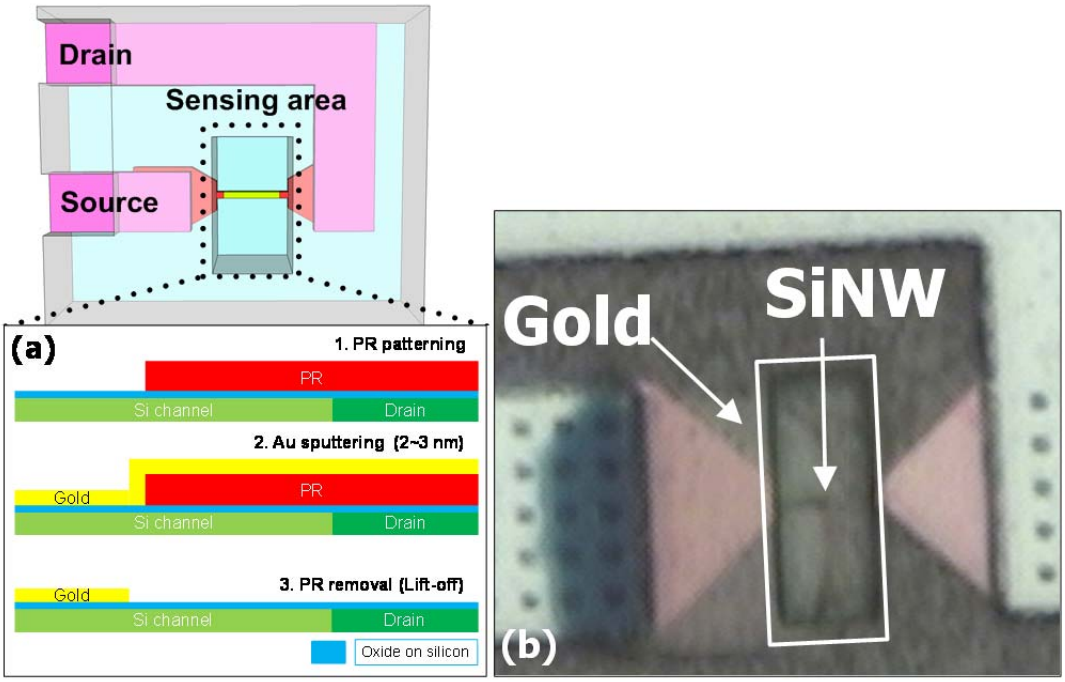

Fig. 5.4. (a) Gold formation process at remaining channel part except for drain edge region. (b) Microscopic top-view image of SiNW sensor parially coverd with gold formed by lift-off process.

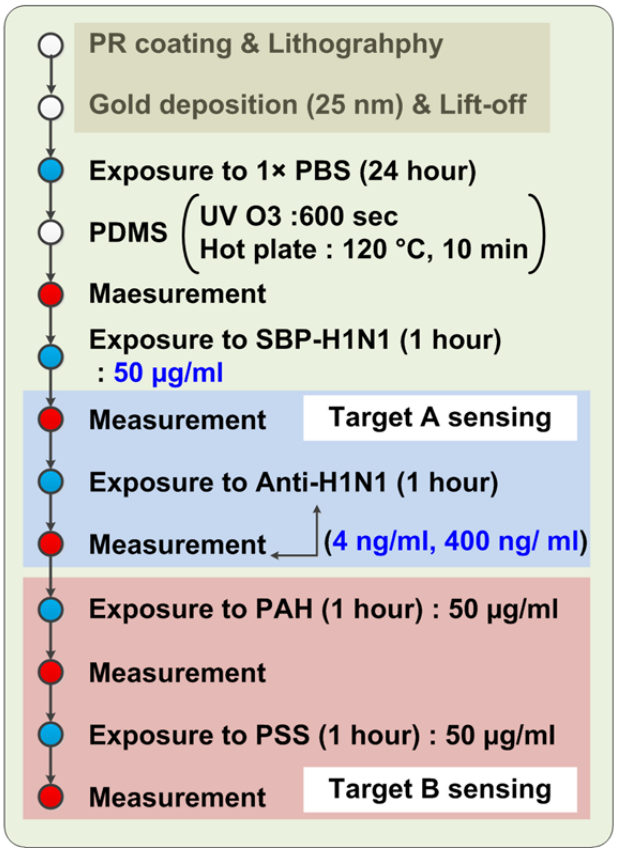

Fig. 5.5. SBP-H1N1/Anit-H1N1 and GBP-Ala/Anti-AI reaction condition and electrical measurement sequence.

Figure 5.5 indicates that biomolecules reaction and electrical measurements are performed as follows. 1) The device is exposed to PBS solution for 24 hours to stabilize the sensor. 2) PDMS is attached to form a fluidic channel as in the previous pH tests, and the electrical characteristics of the initial state of the sensor are measured. 3) The device is exposed to 50 μg/ml SBP-H1N1 selectively bound to silica for one hour. 4) The electrical characteristics of the sensor are measured after SBP-H1N1 is sufficiently

attached to the silica. 5) Similarly, the device is exposed to 40 μg/ml anti-H1N1 (antibody) reacting to SBP-H1N1 (antigen) for one hour and then the change of the electrical characteristics is detected. The same process is repeated for the second target molecules. The device is exposed to 50 μg/ml GBP-AIa selectively reacted with gold, and electrical characteristics are measured. Then, the electrical characteristics are measured by reacting with 40 μg/ml Anti-AI (antibody) binding to GBP-AIa (antigen).

5.4 Multiplexed Sensing Measurements in MOSFET Sensor

First, it is confirmed that SBP-H1N1/GBP-Aia is selectively reacted to gold/SiO_2.

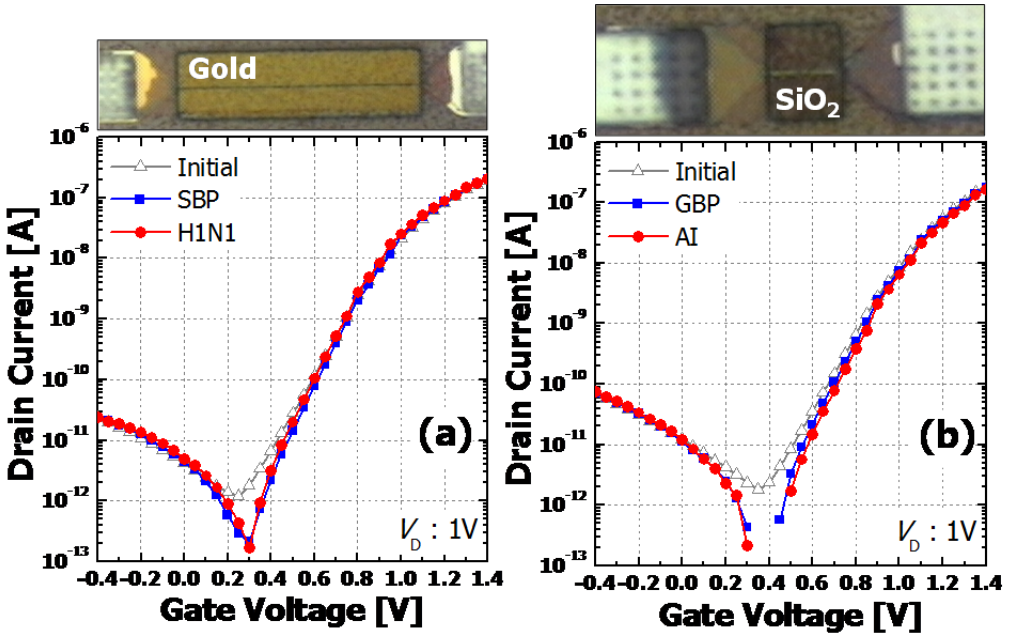

Fig. 5.6 (a) SBP-H1N1/Anti-H1N1 response of MOSFET sensor entirely coated with gold on the sensing area. (b) GBP-AIa/Anti-AI response of MOSFET sensor with SiO_2 on the entire sensing area without gold.

The SBP-H1N1/Anti-H1N1 response of the MOSFET sensor entirely coated with gold on the sensing area is confirmed. The transfer curves of Fig. 5.6(a) show that there is no change in electrical characteristics after the reaction because SBP-H1N1 is selectively reacted with silica and Anti-H1N1 is reacted with SBP-H1N1. In addition, the GBP-AIa/Anti-AI response of the MOSFET sensor having the SiO_2 layer on the whole sensing area without gold is confirmed. There is also no change in electrical properties since GBP-AIa is selectively reacted to the gold and anti-AI is responded only to GBP-AI.

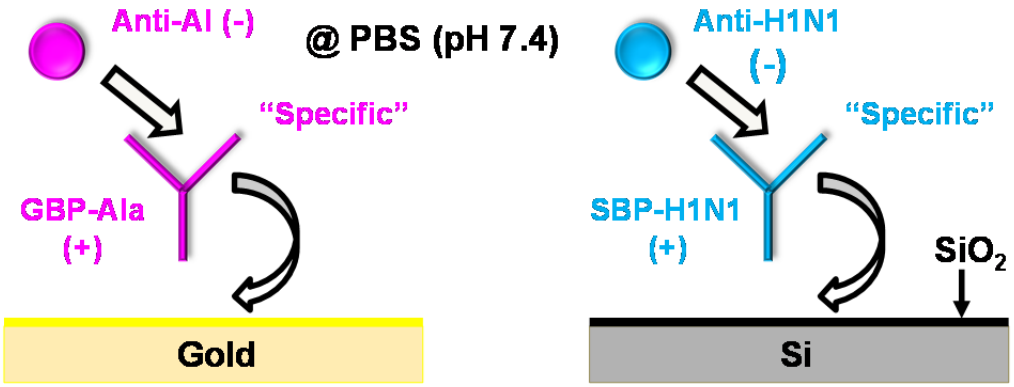

Material	pI value	Material	pI value
GBP-Ala (receptor)	10.02	SBP-H1N1 (receptor)	9.53
Anti-AI (target)	6.02	Anti-H1N1 (target)	6.02

Fig. 5.7. Schematic diagrams to present SBP-H1N1/Anit-H1N1 and GBP-Ala/Anti-AI selectively reacting with gold and SiO_2, respectively and pI value at pH 7.4 (ph of PBS) of each molecule.

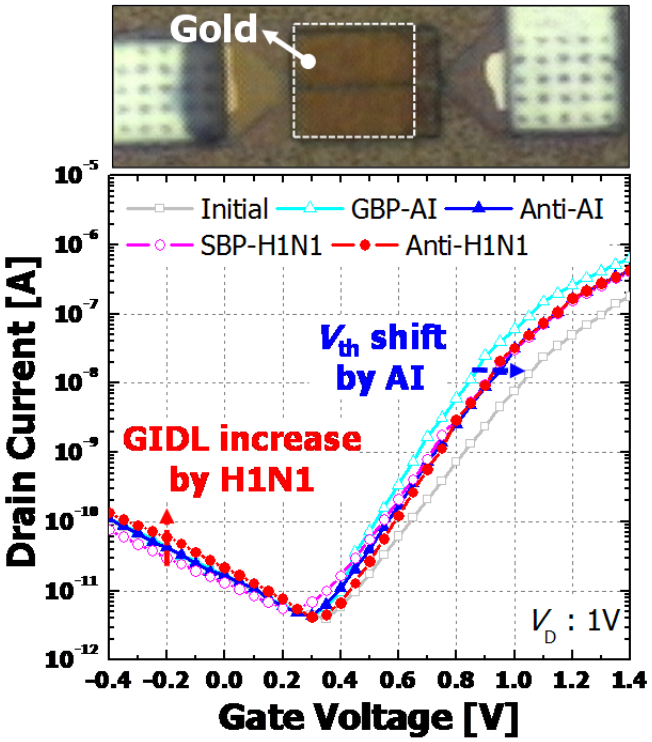

Fig. 5.8. SBP-H1N1/Anti-H1N1 and GBP-AI/Anti-AI responses of the MOSFET sensor coated with gold at remaining channel part except for drain edge.

SBP-H1N1/Anti-H1N1 and GBP-AI/Anti-AI responses of the MOSFET sensor coated with gold at the remaining channel part except for the drain edge are confirmed. When the GBP-AIa/Anti-AI is exposed to the sensor, Figure 5.8 shows that the V_{th} is increased without changing the GIDL because the GBP-AIa/Anti-AI is selectively attached to the gold only. On the other hand, the increase in the GIDL is caused without the V_{th} change since the SBP-H1N1/Anti-H1N1 is selectively attached only to the SiO_2 exposed to the drain edge. Therefore, it is experimentally confirmed that anti-H1N1 and anti-AI can be detected without interference in one MOSFET sensor by forming the

gold layer at the sensing region excluding the drain edge. Moreover, Figure 5.6 proves that these results are well consistent with theoretical expectation when considering the charge polarity of SBP-H1N1/Anit-H1N1 and GBP-Ala/Anti-AI determined by the pl value of each molecule at pH 7.4 (pH of PBS).

5.5 Multiplexed Sensing in TFET Sensor

Although multiple sensing implementations have been identified using MOSFET sensors, the application of MOSFET sensors to multiple sensing systems must involve sophisticated control of the gold forming position.

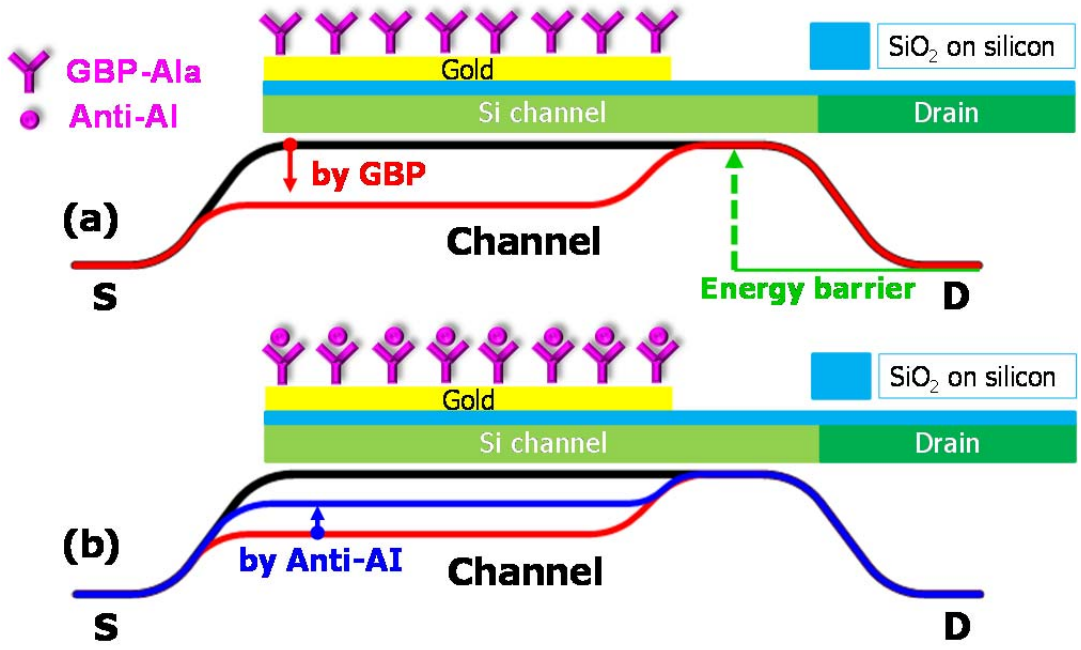

Fig. 5.9. Changes of conduction energy band diagram by (a) attatced GBP-AIa to gold and (b) reacted anti-AI to GBP-AIa, respectively.

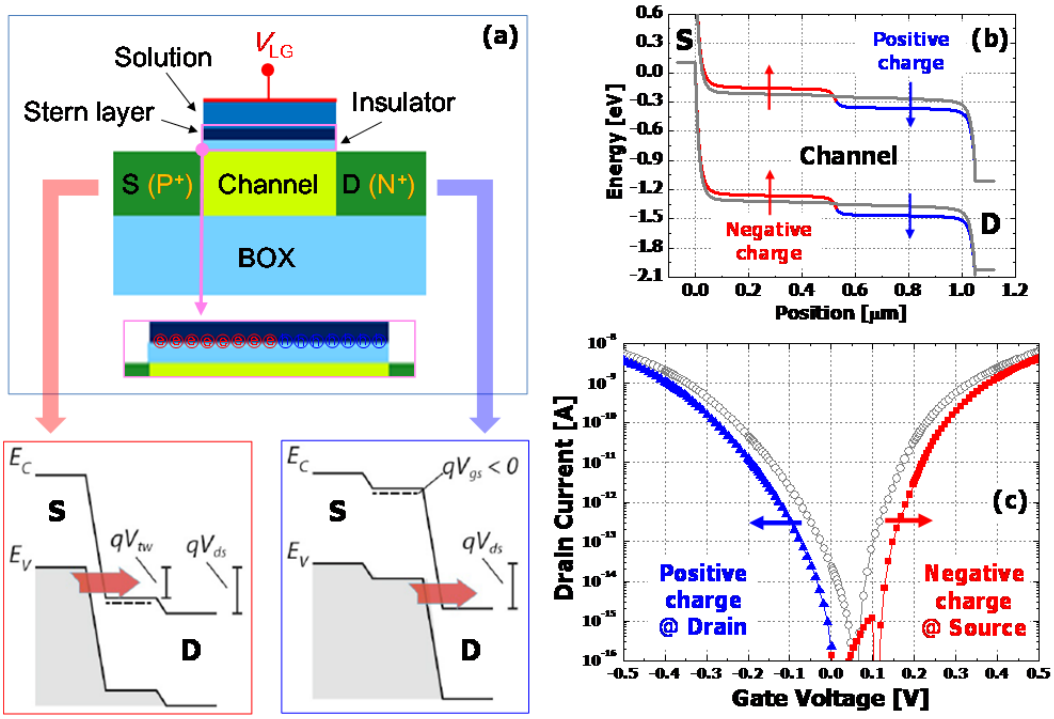

Fig. 5.10. (a) Ambipolar characteristics of TFET sensor. (b) Changes of energy band diagram by different charges on source/drain-side sensing materials. (c) Transfer curves showing multiplexed sensing of biomolecules with opposite charge in one TFET sensor.

As shown in Fig 5.9, if the patterned gold is located far from the drain region, it may have the same energy barrier as the pre-reaction despite the GBP-AIa/Anti-AI reactions, which results in an unchanged V_{th}. This implies that the significant variation of the sensitivity can occur depending on the gold layer position when the GBP-Ala/Anti-AI are attached to the gold, which leads to a reduction in the yield of the multiplexed sensing system. On the other hand, it is possible to perform more stable multiplexed sensing than the MOSFET sensor by using the ambipolar characteristics of the TFET sensor. In addition to BTBT between source and channel at a positive V_G, the

TFET sensor also exhibits channel-to-drain BTBT at a negative V_G as shown in Fig. 5.10(a). Firstly, the multiplexed sensing behavior of the TFET sensor is verified through TCAD simulations. To mimic the binding of two different biomolecules with different charge polarity to each sensing material (source-side gold and drain-side SiO_2), negative charges are attached to the source-side sensing material (Half of the channel) and positive charges are added to the drain-side sensing material (The other half of the channel) as shown in Fig. 5.10(a). As a result, Figure 5.10(c) shows the biomolecule with negative charge can be sensed at positive V_G region, whereas the biomolecule with positive charge can be detected at negative V_G region. Figure 5.10(b) shows the energy band diagrams of the TFET sensor when molecules with different charges are attached to each sensing material. The energy band of the channel is slightly separated. The source side with negative charge is elevated and the drain side with positive charge is moved downward. The mechanism of the multiplexed sensing can be explained by the variation of tunneling barrier thickness at source/channel or channel/drain junction. When a positive V_G is applied (tunneling current), the ascended energy band makes the tunneling barrier thicker between source and channel, which results in the positive-shifted transfer curve at positive V_G region. Likewise, when applying a negative V_G (ambipolar current), the descended energy band prevents electrons from tunneling at channel/drain junction, which leads to the negative-shifted transfer curve at negative V_G region. It should be noted that two different molecules can be sensed at almost equivalent current level by the symmetric nature of the tunneling and ambipolar currents.

In the case of MOSFET sensors, gold should be formed except for the drain edge since the entire channel determines the V_{th} when biomolecules with positive charge are attached to the source-side sensing material. However, the bidirectional currents of the TFET sensor are determined only by the source-to-channel junction and drain-to-channel junction as proved by the transfer curve shifts of Fig. 5.10(c). Therefore, two different biomolecules can be detected independently regardless of the position of the gold layer and thus sufficient margin is achievable in the gold lift off process.

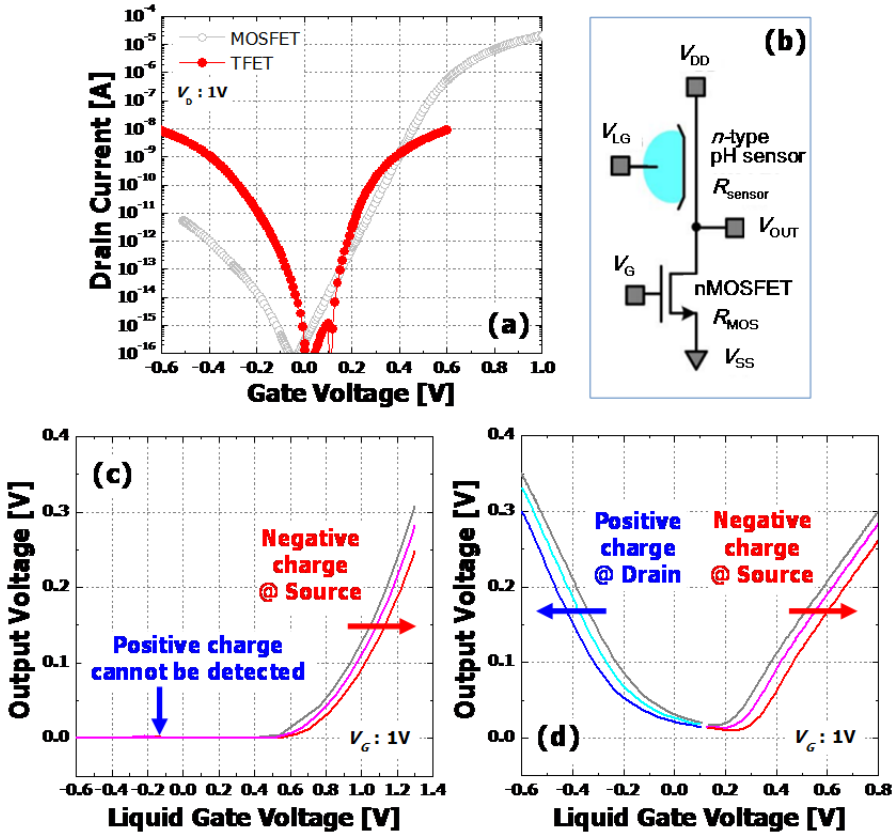

Fig. 5.11. (a) Comparision of transfer curves between MOSFET and TFET sensors. (b) CSA read-out circuit schematic. VTC changes of (c) MOSFET and (d) TFET CSA circuits by negative charge on souce-side gold and positive charge on drain-side SiO_2.

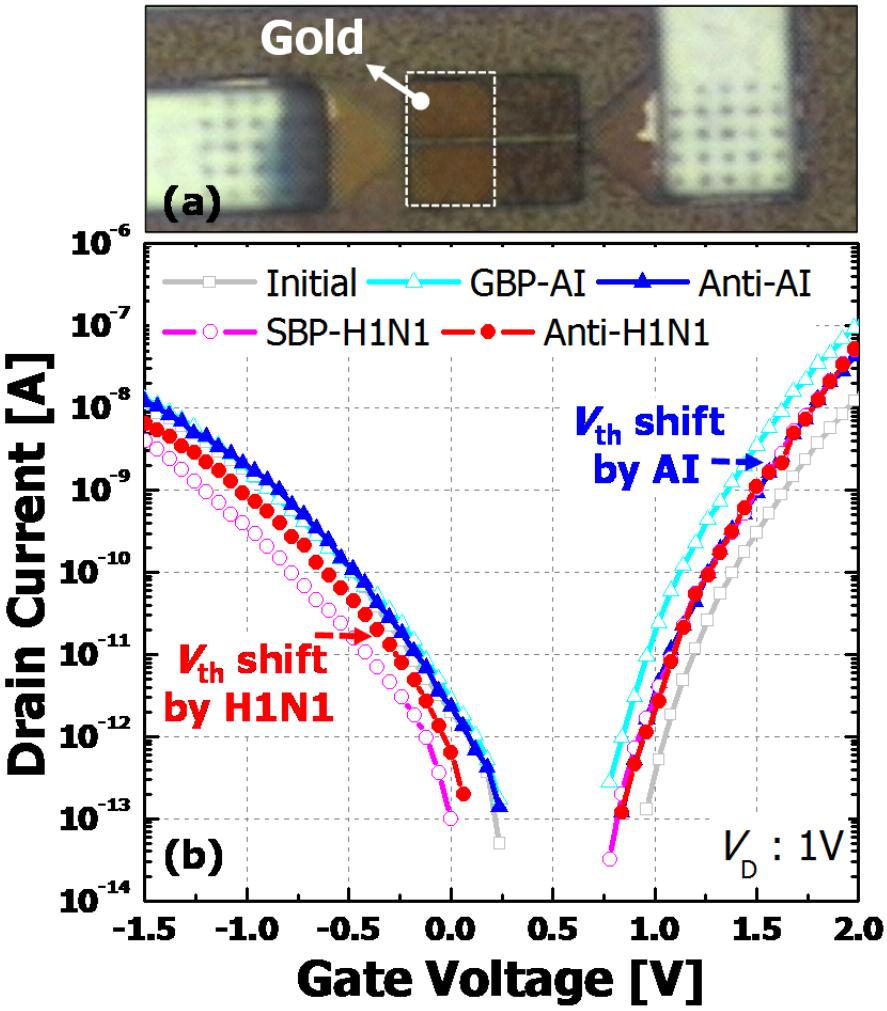

Fig. 5.12. (a) Microscope image of the TFET sensor coated with gold about half of the channel. (b) SBP-H1N1/Anti-H1N1 and GBP-AI/Anti-AI responses of the TFET sensor coated with gold about half of the channel.

For the experiments of multiplexed sensing in the TFET sensor, a gold layer is also formed by the proposed lift-off process. The microscope image of Fig. 5.12(a) shows that the gold is successfully formed about half of the channel. Then, biomolecules reaction

and electrical measurements are performed by the same sequence as that of the MOSFET sensor. As a result, Figure 5.12(b) demonstrates that the tunneling current is increased without the change of the ambipolar current by GBP-AIa/Anti-AI selectively attached to the gold only. On the other hand, the increase in the ambipolar current is caused without changing the tunneling current due to the selective reaction of SBP-H1N1/Anti-H1N1 to the SiO_2. Consequently, it is experimentally confirmed that two different biomolecules can be detected without interference regardless of the position of the gold layer in the TFET sensor. Moreover, it is verified that the multiplexed sensing can be realized in read-out circuits composed of sensor and CMOS, when considering that the tunneling and ambipolar currents of the fabricated TFET sensor are almost equivalent.

Chapter 6

Conclusions

In this dissertation, the novel top-down approached fabrication method using ONO dielectric stacks is proposed and implemented to obtain sensors with defect-free sensing oxide and V_{th}-tunable devices in CMOS read-out circuits. Additionally, as a candidate with higher sensitivity than MOSFET sensors, a TFET sensor is proposed and it is experimentally confirmed that the TFET sensor has the superior sensitivity at SS and saturation regions compared to the MOSFET sensor. Finally, the multiplexed-sensing is realized in one sensor by partially covering gold on SiO_2. GBP-Ala/Anti-AI and SBP-H1N1/Anit-H1N1 are selectively attached to the gold and the SiO_2 and thus two different biomolecules (Anti-AI and Anit-H1N1) are successfully detected without interference in one MOSFET or TFET sensor.

For the implementation of the sensors with defect-free sensing oxide and V_{th}-tunable circuit devices, the etching rate of SiO_2/SiN is first confirmed during H_3PO_4/HF wet-etching, respectively. Then, the sensors with the defect-free sensing oxide are achieved by removing top SiO_2 and SiN from the sensors with the ONO stacks. Despite

the successful formation of the defect-free sensing oxide by the proposed dry + wet etching process, the metal lines are undesirably etched by the HF and the H_3PO_4 during the wet etching. As the solution to prevent the undesirable damage to the metal lines, ONO layer is also used as a passivation layer on the metal lines and the metal lines is completely protected from the wet etching. In terms of the electrical characteristics of the fabricated sensors and circuit devices, the V_{th}-tunability and the retention characteristics of the circuit devices are measured. Moreover, I_D drift and pH response of the sensor are measured and a V_{out} change by SBP-H1N1/Anti-H1N1 is extracted from the CSA circuit including the device with the adjusted V_{th}. As a result, V_{th} shift of 50 mV, improved I_D drift, and V_{out} change of ~ 400 mV is successfully obtained.

Although the defect-free sensing material improves the drift and the sensitivity, the MOSFET sensor has a theoretical limitation on the maximum sensitivity because MOSFETs cannot implement sub-60mV/dec SS at room temperature. To achieve the higher sensitivity, a TFET sensor is proposed and fabricated since it can achieve sub-kT/qS at room temperature by using BTBT as carrier injection mechanism. Through the sensitivity comparison of the fabricated MOSFET and TFET sensors, it is experimentally confirmed that the TFET sensor is the superior sensitivity up to the first I_D saturation region and there is no difference in sensitivity from the second I_D saturation region as compared to the MOSFET sensor.

By using the fabricated MOSFET and TFET sensors, the multiplexed sensing is realized in one sensor. To form two different sensing materials reacted with GBP-

Ala/Anti-AI and SBP-H1N1/Anit-H1N1 for the multiplexed-sensing, gold is partially covered on the SiO_2 by the lift-off process. The changes of saturation and GIDL currents are monitored at the MOSFET sensor after GBP-Ala/Anti-AI (SBP-H1N1/Anit-H1N1) is attached to the gold (SiO_2). Two different biomolecules are independently detected by the changes of the saturation and GIDL currents. To overcome the dependence of the gold formation position on the sensitivity and the dissimilar current level between the saturation and the GIDL currents occurring in the MOSFET sensor, the changes of tunneling and ambipolar currents are measured in the TFET sensor after the antigen-antibody reactions on the gold and the SiO_2. As a result, it is confirmed that two different biomolecules can be detected without interference regardless of the position of the gold layer by the changes of the tunneling and ambipolar currents with almost equivalent current level.

Bibliography

[1] M.-C. Cheng, G. Cuda, Y. L. Bunimovich, M. Gaspari, J. R. Heath, H. D. Hill, C. A. Mirkin, A. J. Nijdam, R. Terracciano, T. Thundat, and M. Ferrari, “Nanotechnologies for biomolecular detection and medical diagnostics,”*Current Opinion Chem. Biol*., vol. 10, no. 1, pp. 11–19, 2006.

[2] N. C. Tansil, and Z. Gao, “Nanoparticles in biomolecular detection,” *Nano Today*, vol. 1, no. 1, pp. 28–37, 2006.

[3] R. J. Lipshutz, S. P. A. Fodor, T. R. Gingeras, and D. J. Lockhart, “High density synthetic oligonucleotide arrays,” *Nature Genet*., vol. 21, pp. 20–24, 1999.

[4] M. Curreli, R. Zhang, F. N. Ishikawa, H. K. Chang, R. J. Cote, C. Zhou, and M. E. Thompson, “Real-time, label-free detection of biological entities using nanowire-based FETs,” *IEEE Trans. Nanotechnol*., vol. 7, no. 6, pp. 651–667, 2008.

[5] X. G. Liang, and S. Y. Chou, "Nanogap detector inside nanofluidic channel for fast real-time label-free DNA analysis," *Nano Lett.*, vol. 8, pp.1472 -1476, 2008.

[6] Y. Chen, X. Wang, M. K. Hong, S. Erramilli, P. Mohanty, and C.

Rosenberg, "Nanoscale field effect transistor for biomolecular signal amplification," *Appl. Phys. Lett.*, vol. 91, no. 24, pp.243511, 2007.

[7] F. Patolsky, G. Zheng, O. Hayden, M. Lakadamyali, X. Zhuang, and C. M. Lieber, "Electrical detection of single viruses," *PNAS*, vol. 101, no. 39, pp. 14017–14022, 2004.

[8] F. Patolsky, G. Zheng, and C. M. Lieber, "Fabrication of silicon nanowire devices for ultrasensitive, label-free, real-time detection of biological and chemical species," *Nature Protocol*, vol. 1, pp. 1711–724, 2006.

[9] K E. Stern, J. F. Klemic, D. A. Routenberg, P. N. Wyrembak, D. B. Turner-Evans, A. D. Hamilton, D. A. LaVan, T. M. Fahmy, and M. A. Reed, "Label-free immune detection with CMOS-compatible semiconducting nanowire," *Nature*, vol. 445, pp. 519–522, 2007.

[10] A. Kim, C. S. Ah, H.Y. Yu, J.-H. Yang, I.-B. Baek, C.-G. Ahn, C. W. Park, and M. S. Jun, "Ultrasensitive, labelfree, and real-time immune detection using silicon field-effect transistors," *Appl. Phys. Lett*., vol. 91, no. 10, pp. 103901, 2007.

[11] K.-S. Shin, K. Lee, J. Y. Kang, and C. O. Chui, "Novel T-Channel Nanowire FET Built-in Signal Amplification for pH Sensing," *IEDM Tech*. *Dig*., pp. 599–602, 2009.

[12] C.-Y. Hsiao, C.-H. Lin, C.-H. Hung, C.-J. Su, Y.-R. Lo, C.-C. Lee, H.-C. Lin, F.-H. Ko, T. Y. Huang, and Y.-S.Yang, "Novel poly-silicon nanowire field effect transistor for biosensing application," *Biosens. Bioelectron*., vol. 24, no. 5, pp. 1223–1229, 2009.

[13] A. Gao, N. Lu, P. Dai, T Li, H. Pei, X. Gao, Y. Gong, Y. Wang, and C. Fan, "Silicon-Nanowire-Based CMOS Compatible Field-Effect Transistor Nanosensors for

Ultrasensitive Electrical Detection of Nucleic Acids," *Nano Lett*., vol. 11, no. 9, pp. 3974–3978, 2011.

[14] Y.-Z. Juang C.-F. Lin, H.-H. Tsai, Y.-K. Su, R.-L. Wang, W.-L. Li, and P.-C. Kung, "A fully compatible CMOS-based hydrogen ion sensor using natural forming sensing membrane for urea detecting application," *Procedia Chemistry*, vol. 1, no. 1, pp. 1067–1070, 2009.

[15] P. Ginet, S. Akiyama, N. Takama, H. Fujita, and B. Kim, "CMOS-compatible fabrication of top-gated field effect transistor silicon nanowire-based biosensors," *J. Micromech. Microeng*., vol. 21, no. 6, pp. 065008, 2011.

[16] W.-Y. Chung, F. G. Cruz, C.-H. Yang, F.-S. He, T.-T. Liu, D. G. Pijanowska, W. Torbicz, P. B. Grabiec, and B. Jarosewicz, "CMOS Readout Circuit Developments for Ion Sensitive Field Effect Transistor Based Sensor Applications," *Solid State Circuits Technologies, Intech, Croatia*, pp. 421–444, 2010.

[17] I. Park, Z. Li, A. P. Pisano, and R. S. Williams, "Top-down fabricated silicon nanowire sensors for real-time chemical detection," *Nanotechnology*, vol. 21, no. 1, pp. 015501, 2009.

[18] O. V. Naumova, B. I. Fomin, D. A. Nasimov, N. V. Dudchenko, S. F. Devyatova, E. D. Zhanaev, V. P. Popov, A. V. Latyshev, A. L. Aseev, Y. D. Ivanov, and A. I. Archakov, "SOI nanowires as sensors for charge Detection," *Semicond. Sci. Technol*., vol. 25, no. 5, pp. 055004, 2010.

[19] J. Lee, J. M. Lee, J. H. Lee, M. Uhm, W. H. Lee, S. Hwang, I. Y. Chung, B. G.

Park, D. M. Kim, Y. J. Jeong, and D. H. Kim, “SiNW-CMOS hybrid common-source amplifier as a voltage-readout hydrogen ion sensor,” *IEEE Electron Device Lett*., vol. 34, no. 1, pp. 135–137, 2013.

[20] J. Lee, J. M. Lee, J. H. Lee, W. H. Lee, M. Uhm, B. G. Park, D. M. Kim, Y. J. Jeong, and D. H. Kim, “Complementary silicon nanowire hydrogen ion sensor with high sensitivity and voltage output,” *IEEE Electron Device Lett*., vol. 33, no. 12, pp. 1768–1770, 2012.

[21] D. W. Kwon, J. H. Lee, S. Kim, R. Lee, H. Mo, J. Park, D. H. Kim, and B. G. Park, “Drift-Free pH Detection With Silicon Nanowire Field-Effect Transistors,” *IEEE Electron Device Lett*., vol. 37, no. 5, pp. 652–655, 2016.

[22] M.-C. Chen, H.-Y. Chen, C.-Y. Lin, C.-H. Chien, T.-F. Hsieh, J.-T. Horng, J.-T. Qiu, C.-C. Huang, C.-H. Ho, and F.-L. Yang, “A CMOS-Compatible Poly-Si Nanowire Device with Hybrid Sensor/Memory Characteristics for System-on-Chip Applications,” *Sensors* ***2012***, vol. 12, no. 4, pp. 3952-3963, 2012.

[23] I. Park, Z. Li, A. P Pisano, and R S. Williams, *“*Top-down fabricated silicon nanowire sensors for real-time chemical detection*,” Nanotechnology*, vol.21, no. 1, pp. 015501, 2010.

[24] Y. Chen, X. Wang, S. Erramilli, P. Mohanty, and A. Kalinowski, **“**Silicon-based nanoelectronic field-effect p H sensor with local gate control,” *Appl. Phys. Lett.*, vol. 89, no. 22, pp. 223512, 2006.

[25] A. Kim, C. S. Ah, H. Y. Yu, J.-H. Yang, I.-B. Baek, C.-G. Ahn, C. W. Park, and M.

S. Jun, “Ultrasensitive, label-free, and real-time immunodetection using silicon field-effect transistors,” *Appl. Phys. Lett*., vol. 91, no. 10, pp.103901, 2007.

[26] P. Ginet, S. Akiyama, N. Takama, H. Fujita, and B. Kim, “CMOS-compatible fabrication of top-gated field-effect transistor silicon nanowire-based biosensors,” *J. Micromech. Microeng*. vol. 21, no. 6, pp.065008, 2011.

[27] W. Y. Choi, B.-G. Park, J. D. Lee, and T.-J. King Liu, “Tunneling field-effect transistors (TFETs) with subthreshold swing (SS) less than 60 mV/dec,” *IEEE Electron Device Lett.*, vol. 28, no. 8, pp. 743–745, 2007.

[28] W. M. Reddick and G. A. J. Amaratunga, “Silicon surface tunnel transistor,” *Appl. Phys. Lett.*, vol. 67, no. 4, pp. 494–496,1995.

[29] K. K. Bhuwalka, S. Sedlmaier, A. K. Ludsteck, C. Toksdorf, J. Schulz, and I Eisele, “Vertical tunnel field effect transistor,” *IEEE Trans Electron Devices*, vol. 51, no. 2, pp. 279–282, 2004.

[30] Q. Zhang, W. Zhao, and A. Seabaugh, “Low-subthreshold-swing tunnel transistors,” *IEEE Electron Device Lett.*, vol. 27, no. 4, pp. 297-300, 2006.

[31] Cui, Q. Wei, H. Park, and C. M. Lieber, “Nanowire nanosensors for highly sensitive and selective detection of biological and chemical Species,” *Science*, vol. 293, no. 5533, pp. 1289–1292, 2001.

[32] F. Patolsky, and C. M. Lieber, “Nanowire nanosensors,” *materialstoday*, vol. 8, no. 4, pp. 20-28, 2005.

[33] H. Jang, J. Lee, J. H. Lee, S. Seo, B.-G. Park, D. M. Kim, D. H. Kim, and I.-Y.

Chung, “Analysis of hysteresis characeristics of SiNW biosensors in aqueous Environment,” *Appl. Phys. Lett*. vol. 99, no. 25, pp. 252103, 2011.

[34] P. Bergveld, “Development of an ion-sensitive solid state device for neurophysiological measurements,” *IEEE Trans. Biomed. Eng.*, vol. BME-17, pp. 70–71, 1970.

[35] P. Bergveld, "Thirty years of ISFETOLOGY - What happened in the past 30 years and what may happen in the next 30 years," *Sens. and Actuators B* : *Chem*., vol. 88, no. 1, pp. 1–20, 2003.

[36] J. M. Rothberg et al., “An integrated semiconductor device enabling non-optical genome sequencing,” *Nature*, vol. 475, no. 7356, pp. 348-352, 2011.

[37] S. Martinoia, G. Massobrio, and L. Lorenzelli, “Modeling ISFET microsensor and ISFET-based microsystems: a review,” *Sensors and Actuators B: chemical*, vol. 49, no. 1, pp. 15-27, 2005.

[38] M. Grattarola and G. Massobrio, “Bioelectronics Handbook: MOSFETs, Biosensors, and Neurons,” Mc Graw Hill (1998), Chapter. 10.

[39] M. Im, J.-H. Ahn, J.-W. Han, T. J. Park, S. Y. Lee, and Y.-K. Choi, “Development of a point-of-care testing platform with a nanogap-embedded separated double-gate field effect transistor array and its readout system for detection of avian influenza,” *IEEE Sensors J*., vol. 11, no. 2, pp. 351–360, 2011.

[40] R. A. Chapman, P. G. Fernandes, O. Seitz, H. J. Stiegler, Y. J. Chabal, and E. M. Vogel, “Comparison of Methods to Bias Fully Depleted SOI-Based MOSFET

Nanoribbon pH Sensors," *IEEE Trans. Electron Devices*., vol. 58, no. 6, pp. 1752-1760, 2011.

[41] B. Choi, J. Lee, J. Yoon, J.-H. Ahn, T. J. Park, D. M. Kim, D. H. Kim, and S.-J. Choi, "TCAD Based Simulation Method for the Electrolye-Insulator-Semiconductor Field-Effect Transistor," *IEEE Trans. Electron Devices*., vol. 62, no. 3, pp. 1072-1075, 2015.

[42] M. T. Bjork, J. Knoch, H. Schmid, H. Riel, and W. Riess, "Silicon nanowire tunneling field-effect transistor," *Appl. Phys. Lett.*, vol. 92, no. 19, pp. 193-504, 2008.

[43] V. Nagavarapu, R. Jhaveri, and J. C. S. Woo, "The tunnel source (PNPN) n-MOSFET: A novel high performance transistor," *IEEE Trans. Electron Devices*, vol. 55, no. 4, pp. 1013–1019, 2008.

[44] R. Gandhi, Z. X. Chen, N. Singh, K. Banerjee, and S. J. Lee, "Vertical Sinanowire n-type tunneling FETs with low subthreshold swing (≤ 50 mV/ decade) at room temperature," *IEEE Electron Device Lett.*, vol. 32, no. 4, pp. 437-439, 2011.

[45] E. O. Kane, "Theory of tunneling," *J. Appl. Phys.*, vol. 32, no. 1, pp. 83-91, 1961.

[46] Sze, S. M, "Physics of Semiconductor Devices," 1st edn, John Wiley, 1969.

[47] I.-Y. Chung, H. Jang, J. Lee, H. Moon, S. M. Seo, and D. H. Kim, "Simulation study on discrete charge effects of SiNW biosensors according to bound target position using a 3D TCAD simulator," *Nanotechnology*, vol. 23, no. 6, pp. 065202, 2012.

[48] D. Sarkar, H. Gossner, W. Hansch, and K. Banerjee, "Tunnel-field-effect-transistor based gas-sensor: introducing gas detection with a quantum-mechanical transducer,"

Appl. Phys. Lett., vol. 102, no. 2, pp. 023110, 2013.

[49] G. Zheng, F. Patolsky, Y. Cui, W.U. Wang and C. M. Lieber, "Multiplexed electrical detection of cancer markers with nanowire sensor arrays," *Nat. Biotechnol*, vol. 23, no. 10, pp. 1294–301, 2005.

[50] J.-Y. Kim, J.-H. Ahn, D.-I. Moon, T. J. Park, S. Y. Lee, and Y.-K. Choi, "Multiplex electrical detection of avian influenza and human immunodeficiency virus with an underlap-embedded silicon nanowire field-effect transistor," *Biosensors Bioelectron.*, vol. 55, pp. 162–167, 2014.

초록

제조 기술이 계속 개발됨에 따라 센서의 크기가 DNA, 단백질, 바이러스와 같은 생물체의 크기와 비슷해지기 때문에 다양한 나노크기의 생물 의학 센서가 널리 연구되어왔다. 특히, 형광 표지 및 광학 검출 기술을 이용한 화학 및 생물 의학 센서는 높은 민감도로 인하여 많은 주목을 받았다. 그러나, 샘플 준비 및 데이터 분석이 값 비싸고 프로세스가 시간 소모적인 단점이 있다.

이러한 제한을 극복하기 위해, 라벨이 없는 실시간 감지 및 우수한 감도와 같은 특성을 가지는 실리콘 나노와이어 이온 감지 전계 효과 트랜지스터 (SiNW ISFET)가 가장 유망한 화학/생물 의학 센서 중 하나로 제안되었다. SiNW ISFET는 표면 대 부피 비율이 높기 때문에 우수한 감도를 가지며 제조 공정 측면에서 CMOS 기술과도 호환된다. 이와 관련하여 SiNW ISFET의 다양한 제조 방법이 보고되고 있으며 최근 우리 그룹은 top-down 제조 공정을 사용하여 CMOS 소자와 공동 집적 될 수 있는 새로운 SiNW MOSFET 센서를 구현했다. 그러나 제안 된 공정은 감지 영역이 건식 에칭 공정에 의해 형성되어 플라즈마에 의한 감지 재료의 손상을 피할 수 없으며 이는 감도와 전류 드리프트의 저하를 초래한다. 또한, 임플란트 공정으로 회로 소자의 다양한 문턱 전압을 미세 조정하는 것은 불가능하며, 이는 회로 오작동 및 증폭 인자의 감소를 가져온다.

본 논문에서는 상층 실리콘 산화막-실리콘 질화막-하층 실리콘 산화막 (ONO) 유전체 스택을 이용한 새로운 하향식 제조 방법을 제안하고 구현하여 무 결함 감지 산화물을 가지는 센서 및 CMOS 판독 회로에서 문턱전압이 가변 가능한 디바이스를 확보하는 것을 목표로 한다. 상부 실리콘 산화막 및 실리콘 질화막을 습식 에칭함으로써, 무 결함 감지 산화물을 갖는 센서가 얻어진다. 또한, ONO 적층을 갖는 문턱전압 가변 가능한 회로 소자는 ONO 적층을 습식 에칭으로부터 보호함으로써 동시에 확보 가능하다. 센서 소자의 pH 응답과 전류 드리프트 측정 및 회로 소자의 프로그램 동작 측정을 통해 센서의 pH/생체 분자 반응 및 전류 드리프트가 무 결함 감지 산화물로 인하여 향상되고 회로 소자의 문턱전압이 미세하게 제어 될 수 있음이 실험적으로 확인되었다.

무 결함 감지 재료가 드리프트와 감도를 향상 시키지만, MOSFET 센서에서는 상온에서 60mV/dec 미만의 subthreshold swing (SS)를 구현할 수 없으므로 최대 감도에 이론적인 한계가 있다. 더 높은 감도를 얻기 위해, TFET 센서가 제안되고 제작되었다. 이는 캐리어 주입 메커니즘으로서 band-to-band tunneling (BTBT)을 사용함으로써 TFET 센서에서는 상온에서 sub-kT/qS를 달성 할 수 있기 때문이다. TCAD 시뮬레이션으로부터, TFET 센서는 소스 채널간 터널링 폭 포화 및 드레인으로부터 캐리어 주입으로 인하여 두 번의 드레인 전류포화를 갖는 것으로 밝혀졌다. 또한, MOSFET 센서와 비교하여 TFET 센서는 첫 번째 전류포화 영역까지 우수한 감도를 가지며, 두 번째 전류포화 영역부터는 감도에 차이가 없다는 것이 실험적으로

확인되었다.

마지막으로, 다중 감지의 가능성이 제작 된 MOSFET 및 TFET 센서로 검증되었다. 다중 감지를 위해 GBP-Ala/Anti-AI 및 SBP-H1N1/Anit-H1N1과 반응하는 두 개의 서로 다른 감지 재료를 형성하기 위해 금을 리프트 오프 공정으로 실리콘 산화막 위에 부분적으로 덮었다. 그리고 GBP-Ala/Anti-AI (SBP-H1N1/Anit-H1N1)와 금 (실리콘 산화막)을 반응시킨 후 MOFET 센서에서 포화전류와 GIDL전류의 변화를 확인했다. 두 개의 다른 생체 분자는 포화전류와 GIDL전류의 변화에 의해 독립적으로 검출 가능함이 확인 되었다. 감도에 대한 금 형성 위치의 영향과 포화 전류와 GIDL전류 사이의 큰 전류 차에 의한 MOSFET 센서의 문제를 해결하기 위해 TFET 센서에서는 터널링과 양극성 전류의 변화가 측정되었다. 그 결과 거의 동일한 전류 준위을 가지는 양극성 전류 및 터널링 전류의 변화에 의해 금의 위치와 관계없이 두 개의 다른 생체 분자가 간섭 없이 검출 될 수 있음이 밝혀졌다.

주요어: 무 결함 감지 재료를 가지는 ISFET, 터널링전계효과트랜지스터 바이오센서, 다중 감지, 양방향 전류를 이용한 다중감지.

학번: 2014-30316